# The Interior of Enceladus

**Douglas Hemingway**
*University of California, Berkeley*

**Luciano Iess**
*Università La Sapienza, Rome*

**Radwan Tajeddine**
*Cornell University*

**Gabriel Tobie**
*Université de Nantes*

Knowledge of internal structure places constraints on the origin, evolution, and present behavior of Enceladus. Although the interior cannot be observed directly, much can be deduced from the magnitude of tidal and rotational asymmetries in the shape and gravity field and from how these asymmetries affect the rotational dynamics. The data and models suggest a differentiated interior consisting of a ~2400 kg m$^{-3}$ rocky core, a 20–50-km mean thickness global subsurface liquid water ocean, and a 20–30-km mean thickness icy shell. The presence of an internal liquid water reservoir had been suggested by a series of observations early in the Cassini mission and was ultimately confirmed by two crucial and independent analyses related to (1) determination of Enceladus' low-order gravity field based on Doppler tracking of the Cassini spacecraft during dedicated flybys and (2) measurement of forced physical librations based on control point tracking through seven years of Cassini images. Although Cassini-based observations have yielded a good, basic picture of the interior of Enceladus, many unresolved issues remain — in particular, relating to the structure and stability of the icy shell and related implications for the energy budget and thermal evolution of Enceladus — and will need to be addressed through further modeling and, eventually, additional observations.

## 1. INTRODUCTION

### 1.1. Motivation

The internal structure of a planetary body provides essential clues about its origin and evolution. Based on its internal density structure, what is the likely composition of the materials from which the body formed (see the chapter in this volume by McKinnon et al.)? Did the interior become sufficiently warm to enable differentiation, with heavier components sinking toward the center? How quickly or slowly did the body form? What does the structure of the near surface and deeper interior tell us about the nature of the topography and the distribution of geologic provinces across the surface?

The interior of Enceladus is of particular interest because of the complex tectonic structures that cover much of its unusually youthful surface (see chapter in this volume by Patterson et al.) and, most strikingly, because of the ongoing eruptions of water vapor and ice grains from its south

polar region (see chapters in this volume by Postberg et al., Goldstein et al., and Spencer et al.). Are these eruptions sourced from a potentially habitable subsurface liquid water reservoir? If so, how deep is the reservoir beneath the icy surface? How thick is the icy crust? What is the structure of the crust and how does it support the surface topography? How is the liquid water, which is not buoyant with respect to the ice, transported to the surface? How does the interior respond to tidal stresses? What modulates the eruptive activity at the south pole? How large is the internal sea or ocean, and how does it keep from freezing solid? What is the composition and nature of the core, and what is its capacity for contributing to the heating of the interior?

Although the internal structure cannot be observed directly, a variety of techniques are available for building a picture of the interior that can help to address many of these questions. Seismic imaging has proven to be the definitive technique for constraining the structure of Earth's interior, and seismic stations placed on the Moon during the Apollo program have likewise helped to improve our understanding

of the Moon's interior. However, although seismic stations may soon be deployed on Mars and other worlds, the study of planetary interiors aside from Earth and the Moon has so far had to rely on other methods. In particular, as we will discuss in detail in this chapter, studies of shape, gravitational fields, and rotational dynamics can place constraints on planetary interiors, and have enabled significant advancements in our emerging understanding of Enceladus.

## 1.2.  Key Observations and Basic Picture

Prior to the Cassini spacecraft's arrival in the Saturn system in 2004, our knowledge of Enceladus was limited to what could be inferred from telescopic observations and the data collected during the Saturn system flybys of Pioneer 11 in 1979 and the two Voyager spacecraft in 1980 and 1981. However, even these early observations led to considerable interest in Enceladus due to its unusually high albedo (*Buratti and Veverka,* 1984) and apparently youthful icy surface (*Smith et al.,* 1982; *Clark et al.,* 1983; *Squyres et al.,* 1983), as well as its relationship to Saturn's E ring (*Baum et al.,* 1981; *Haff et al.,* 1983; *Pang et al.,* 1984), all of which pointed to the incredible possibility of recent, or even ongoing, geologic activity on this tiny moon. Given the apparent history of geologic activity, and incorporating mass estimates based on astrometric observations (*Kozai,* 1976; *Jacobson,* 2004), basic interior models were developed for a differentiated Enceladus (*Zharkov et al.,* 1985), but were limited by the large uncertainties regarding its size and shape.

Beginning in 2005, the Cassini mission, which included numerous flybys of Enceladus, led to a series of remarkable observations that reinforced Enceladus' status as one of the most compelling exploration targets in the solar system, and provided clues about the nature of its interior. In particular, several of Cassini's instruments detected water vapor and organic molecules in the vicinity of Enceladus' south pole (*Brown et al.,* 2006; *Dougherty et al.,* 2006; *Hansen et al.,* 2006; *Spahn et al.,* 2006; *Spencer et al.,* 2006; *Waite et al.,* 2006), and spectacular back-lit images revealed the source of this material to be a series of ongoing eruptions concentrated along four major fissures spanning the highly tectonized south polar terrain (SPT) (*Porco et al.,* 2006). Subsequent observations identified high heat flow emanating from the south polar region and especially at the sites of the most prominent eruptions (*Spitale and Porco,* 2007; *Howett et al.,* 2011). The ongoing activity led to the suggestion that a subsurface sea might be feeding the eruptions (*Collins and Goodman,* 2007) and producing a topographic depression at the south pole, helping to explain the anomalous shape (*Thomas et al.,* 2007). The finding that the erupted ice grains contained salts (*Postberg et al.,* 2009, 2011) further supported the notion of an internal liquid water reservoir. On the other hand, the limited presumed available tidal heating energy (*Meyer and Wisdom,* 2007), together with the rapid heat loss, suggested that an internal sea should have frozen solid in just tens of millions of years (*Roberts and Nimmo,* 2008).

A major advancement in our knowledge of the interior came with Doppler tracking of the Cassini spacecraft during close encounters with Enceladus (*Rappaport et al.,* 2007), and especially with the determination of Enceladus' quadrupole gravity field and hemispherical asymmetry, once enough flyby results had been accumulated (*Iess et al.,* 2014). In combination with improved models of the topography (*Thomas et al.,* 2007; *Nimmo et al.,* 2011), the gravity data provided the first opportunity to effectively probe the interior, yielding an estimate of the degree of differentiation, and identifying mass anomalies suggestive of a (possibly global) subsurface liquid ocean. Subsequent measurement of the forced physical librations (*Thomas et al.,* 2016) independently confirmed that the icy crust must be fully decoupled from the deep interior, indicating that the internal ocean must indeed be global. Although detailed interpretation of these observations is complicated and remains an active area of research (e.g., *Čadek et al.,* 2016, 2017; *van Hoolst et al.,* 2016; *Beuthe et al.,* 2016; *Hemingway and Mittal,* 2017), the general conclusion is that Enceladus is differentiated, with an icy shell covering a global subsurface liquid water ocean, overlying a low-density rocky core (Fig. 1).

In this chapter, we examine the relevant theory and discuss the constraints that can be placed on the internal structure of Enceladus based mainly on the gravity and libration observations (sections 2 and 3, respectively). We also discuss the implications for the thermal state of Enceladus and, in particular, the structure and dynamics of its icy shell (section 4). Finally, we discuss the remaining open
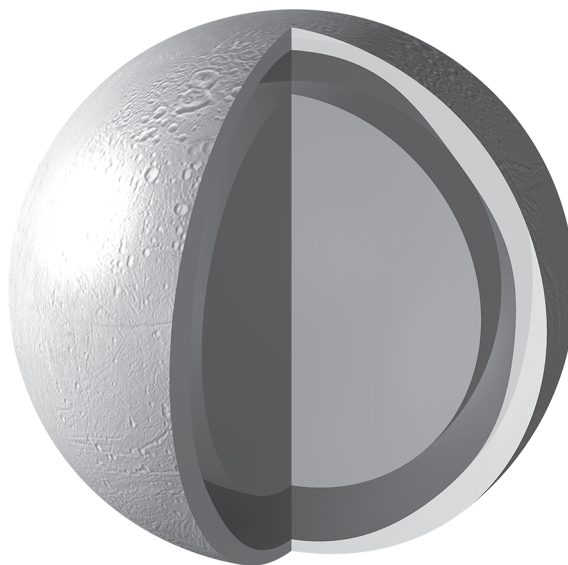


**Fig. 1.** Approximate interior structure of Enceladus (to scale). Its 252-km radius comprises a ~190-km-radius core with a density of ~2400 kg m$^{-3}$, surrounded by layers of liquid and solid $H_2O$ making up the remaining ~60 km. The ice shell and ocean layer thicknesses vary laterally, with the thinnest part of the ice shell (and thickest part of the ocean) being centered on the south pole (see Table 3).

questions and how future observations and modeling might help to address them (section 5).

## 2. IMPLICATIONS FROM GRAVITY

Gravity is a powerful tool for studying planetary interiors because a body's gravitational field is ultimately a function of its internal mass distribution. While the problem of inverting gravity for interior structure suffers from inherent non-uniqueness, with a few reasonable assumptions, it is nevertheless possible to draw useful conclusions. For example, it is often reasonable to assume that large planetary bodies have interiors that are weak on long timescales, meaning that they tend to relax to near spherical symmetry, and that their internal densities do not generally increase with radial position — a situation that would be gravitationally unstable.

A straightforward approach to interior modeling is therefore to treat the body as a series of concentric spherical shells of different densities, with the requirement that the densities increase monotonically inward. The mean density, $\bar{\rho}$, of such a body is given by

$$\bar{\rho} = \sum_i \Delta\rho_i \left(\frac{R_i}{R}\right)^3 \tag{1}$$

where R is the body's full radius, $R_i$ is the outer radius of the ith layer, and $\Delta\rho_i$ is the density contrast between layer i and the layer above it. This formulation implicitly assumes uniform density within each layer, which is appropriate only when internal pressures are small enough not to cause significant compression. For larger bodies, where compression may be important, equations of state are required to model the radial dependence of density on temperature and pressure. We proceed here assuming that compression is not important in the interior of Enceladus.

The body's normalized mean moment of inertia (or moment of inertia factor) is given by

$$\frac{I}{MR^2} = \frac{2}{5}\sum_i \frac{\Delta\rho_i}{\bar{\rho}} \left(\frac{R_i}{R}\right)^5 \tag{2}$$

Although there are generally more than two unknowns, necessitating additional assumptions, these two equations provide fundamental constraints on the internal structure. The mean density can be determined directly from the mass and radius, and immediately restricts the range of possible bulk compositions. But the moment of inertia, which reflects density stratification, must be determined via other means.

The three principal moments of inertia can be defined as

$$A = \int \rho\left(y^2 + z^2\right)dV$$

$$B = \int \rho\left(x^2 + z^2\right)dV \tag{3}$$

$$C = \int \rho\left(x^2 + y^2\right)dV$$

where $\rho$ is the density of a volume element dV, at position x, y, z within the body. Here, the principal frame is a coordinate frame centered on the body with the z-axis coincident with the spin pole, the x-axis pointing toward the prime meridian, and the y-axis completing the righthanded system (for synchronous satellites in circular orbits, the x-axis points along the long axis, toward the parent body). Differences in these principal moments of inertia are important because they can, in some cases, be related to observable rotational dynamical effects such as spin pole precession, obliquity, nutation, and librations (e.g., *van Hoolst,* 2015) — the subject of section 3 of this chapter; or to asymmetries in the gravitational field — the subject of the rest of this section. In the limit of perfect spherical symmetry, a body's gravitational field would be equivalent to that of a point mass located at its center and, apart from the mean density, little could be concluded about the interior. Real planetary bodies, however, exhibit asymmetries that effectively carry information about their internal structures.

The case of Enceladus is interesting and instructive for several reasons. Because of the short period of its orbit around Saturn (1.37 days), the asymmetries in its shape and gravity (primarily due to tidal and rotational deformation) are large, permitting unprecedented relative precision in their measurement. This precision presents both challenges (it forces us to abandon the usual simplifying assumption of hydrostatic equilibrium) and opportunities (it allows us to estimate the thickness of the icy crust via analysis of the non-hydrostatic gravity and topography), forcing the development of new methods for interior modeling from shape and gravity (*Hemingway et al.,* 2013b; *Iess et al.,* 2014; *McKinnon,* 2015; *Čadek et al.,* 2016; *Beuthe et al.,* 2016). Finally, the special circumstance of the substantial north-south polar asymmetry associated with the SPT provides an opportunity for independent analysis of long-wavelength gravity and topography.

In section 2.1, we discuss how rotational and tidal effects lead to characteristic asymmetries in a body's shape and, consequently, its gravitational field, and how the magnitude of those asymmetries is related to the internal mass distribution. To do this, we introduce several concepts, including gravitational potential and the ways it is affected by tidal and rotational forces; hydrostatic equilibrium figure theory; and Love numbers and their connection to the principal moments of inertia and, ultimately, the density stratification within the body. In section 2.2, we discuss how the gravitational field of Enceladus has been measured based on radio tracking of the Cassini spacecraft during three close flybys. Finally, in section 2.3, we discuss the interpretation of those measurements, including some of the subtleties and challenges associated with interior modeling.

### 2.1. Theory

***2.1.1. Hydrostatic equilibrium.*** For planetary bodies that are sufficiently large, the combination of high internal pressures and low internal viscosities (especially true when

there is appreciable internal heating) results in relaxation to a figure that approaches the expectation for a strengthless fluid body, in which the inward acceleration due to gravity is everywhere balanced by the gradient in fluid pressure — a condition referred to as hydrostatic equilibrium and described by the equation $dp = -\rho g dr$, where p, $\rho$, g, and r are the pressure, local density, local gravity, and radial position, respectively.

Under the influence of self-gravitation alone, the hydrostatic equilibrium figure would be a sphere. Because of their rotation, however, planetary bodies also experience centrifugal flattening. In addition, satellites that are in synchronous rotation with their parent bodies (i.e., tidally locked) also experience permanent elongation along the static tidal axis. This applies to most of the large natural satellites in the solar system because of the short timescale associated with tidal locking (e.g., *Gladman et al.,* 1996; *Murray and Dermott,* 1999). The tidal and rotational deformation results in an asymmetry in the equilibrium figure — and consequently the gravitational field — of synchronous satellites like Enceladus.

***2.1.2. Gravitational potential.*** A body's Newtonian gravitational potential, U, resolved at an arbitrary position **r**, is a function of its internal mass distribution, and is given by

$$U(\mathbf{r}) = -G \int_V \frac{\rho(\mathbf{r}')}{|\mathbf{r}-\mathbf{r}'|} dV' \tag{4}$$

where $\rho(\mathbf{r}')$ is the density at position $\mathbf{r}'$, where G is the universal gravitational constant, and where the integral is performed over the body's entire volume, V. The potential represents the work per unit mass done by the gravitational field and gives rise to the gravitational acceleration $\mathbf{g} = -\nabla U$.

Everywhere outside the body, the gravitational potential satisfies Laplace's equation, $\nabla^2 U(r) = 0$, and can be expressed as a linear combination of spherical harmonic functions as

$$U(r,\theta,\phi) = -\frac{GM}{r} \sum_{l=0}^{\infty} \sum_{m=-l}^{l} \left(\frac{R_{ref}}{r}\right)^l C_{lm} Y_{lm}(\theta,\phi) \tag{5}$$

where M is the total mass of the body, r is the radius at which the potential is to be expressed, $\theta$ is colatitude, $\phi$ is longitude, $C_{lm}$ are the degree-l and order-m spherical harmonic expansion coefficients representing the dimensionless gravitational potential at the reference radius $R_{ref}$, and where $Y_{lm}$ are the spherical harmonic functions — the natural set of orthogonal basis functions on a sphere (e.g., *Wieczorek,* 2015).

***2.1.3. Tidal/rotational disturbing potential.*** The tidal and rotational forces that cause planetary bodies to deviate from spherical symmetry can be described in terms of disturbances in the potential field. For instance, the centrifugal acceleration at a point on the surface of a spherical body with radius R and spin rate $\omega$ is $\omega^2 x$, where $\mathbf{x} = R \sin\theta \, \hat{\mathbf{x}}$ is a vector pointed outward from, and perpendicular to, the axis of rotation and reaching the surface at colatitude $\theta$. This acceleration can be expressed as the negative gradient of a centrifugal disturbing potential, $-\nabla V^{cf}$, where

$$V^{cf} = -\tfrac{1}{2}\omega^2 R^2 \sin^2\theta \tag{6}$$

For convenient comparison with equation (5), we can rewrite the centrifugal disturbing potential in terms of the degree-2 Legendre polynomial, $P_2(\cos\theta) = \tfrac{1}{2}(3\cos^2\theta - 1)$, as $V^{cf}(\theta,\phi) = \tfrac{1}{3}\omega^2 R^2 (P_2(\cos\theta)-1)$. Since the last term is a constant, its gradient is zero, meaning that it gives rise to no deforming forces. As such, many authors do not include it, and we will likewise disregard it from here on. Finally, we can write the centrifugal disturbing potential (excluding the constant term) in terms of the degree-2 zonal spherical harmonic function, $Y_{20}(\theta,\phi)$, as

$$V^{cf}(\theta,\phi) = \tfrac{1}{3}\omega^2 R^2 Y_{20}(\theta,\phi) \tag{7}$$

In addition to the effects of rotation, satellites experience a tidal disturbing potential due to the spatially varying difference between their gravitational acceleration toward the parent body and the outward centrifugal acceleration associated with their orbital motion. To second order, it can be shown (e.g., *Murray and Dermott,* 1999, p. 133) that the net tidal disturbing potential is

$$V^{tid}(\psi) = -\frac{GmR^2}{a^3} P_2(\cos\psi) \tag{8}$$

where m is the mass of the parent body, a is the distance between the centers of the two bodies, and $\psi$ is the angle from the axis connecting the centers of the two bodies to an arbitrary point on the satellite's surface. If the parent body is much more massive than the satellite ($m \gg M$), and the satellite's orbit is synchronous with its mean rotation rate, then $\omega^2 \approx Gm/a^3$. And if the satellite's spin axis is nearly normal to its orbital plane (i.e., its obliquity is close to zero), then we can rewrite the angle $\psi$ in terms of colatitude and longitude as $\cos\psi \approx \cos\phi \sin\theta$. Both of these conditions are satisfied in the present case because Saturn is more than a million times as massive as Enceladus, whose obliquity is <0.001 (*Chen and Nimmo,* 2011; *Baland et al.,* 2016). Incorporating these approximations, it can be shown that

$$V^{tid}(\theta,\phi) = \omega^2 R^2 \left( \tfrac{1}{2} Y_{20}(\theta,\phi) - \tfrac{1}{4} Y_{22}(\theta,\phi) \right) \tag{9}$$

Adding equations (7) and (9) yields the combined effect of the tidal and rotational disturbing potentials

$$V(\theta,\phi) = \omega^2 R^2 \left( \tfrac{5}{6} Y_{20}(\theta,\phi) - \tfrac{1}{4} Y_{22}(\theta,\phi) \right) \tag{10}$$

***2.1.4. Equilibrium figure theory.*** To the extent that the body can be treated as a hydrostatic fluid, its equilibrium figure will conform to an equipotential. The effect of the disturbing potential, $V(\theta,\phi)$, is that the surface of the initially spherically symmetric body will no longer be equipotential. To first order, and before any deformation has taken place, the resulting change in elevation of the equipotential surface is $-V(\theta,\phi)/g$ (since g is the gradient of the gravitational potential). In response to the disturbing potential, the body's

figure will relax toward the new equipotential surface. However, in so doing, the body's mass distribution is altered, effectively causing a small additional disturbance in the gravitational potential. Accounting for this self-gravitation effect, the hydrostatic equilibrium figure can be written

$$H(\theta, \phi) = R - \frac{V(\theta, \phi)}{g} h_f \qquad (11)$$

where $h_f$ is the fluid Love number for the figure, a scalar quantity describing the magnitude of the body's long timescale (zero frequency) deformation in response to the disturbing potential. An infinitely rigid body would have $h_f = 0$, whereas a perfectly homogeneous fluid body has $h_f = \frac{5}{2}$ (the value is larger than unity because of the aforementioned self-gravitation); fluid bodies with some internal density stratification have $0 < h_f < \frac{5}{2}$. The resulting asymmetries in the gravitational potential are given by

$$U(\theta, \phi) = V(\theta, \phi) k_f \qquad (12)$$

which defines the potential fluid Love number $k_f$. For perfectly fluid bodies, $h_f = 1 + k_f$. The fluid Love numbers are of great importance for interior modeling because they can be related to the body's internal density distribution, as discussed in the next section. Since the disturbing potential in equation (10) is a degree-2 spherical harmonic function, we are here concerned with the degree-2 fluid Love numbers, $h_{2f}$ and $k_{2f}$.

Note that the fluid Love numbers should not be confused with the tidal Love numbers, which characterize the body's viscoelastic response in both shape ($h_{2t}$) and gravitational potential ($k_{2t}$) due to eccentricity tides — variations in tidal potential associated with the body's changing proximity to its parent body. Ignoring these short-timescale variations in shape and gravity, a synchronous satellite in hydrostatic equilibrium thus has a mean figure described by

$$H(\theta, \phi) = R - Rqh_{2f} \left( \frac{5}{6} Y_{20}(\theta, \phi) - \frac{1}{4} Y_{22}(\theta, \phi) \right) \qquad (13)$$

and a gravitational field whose asymmetries are described by

$$U(\theta, \phi) = \frac{GM}{R} qk_{2f} \left( \frac{5}{6} Y_{20}(\theta, \phi) - \frac{1}{4} Y_{22}(\theta, \phi) \right) \qquad (14)$$

where we have introduced the commonly used parameter

$$q = \frac{\omega^2 R}{g} = \frac{mR^3}{Ma^3} \qquad (15)$$

representing the relationship between the inward gravitational acceleration and the outward centrifugal acceleration at the body's equator.

It is clear from equation (14) that, for a synchronous satellite in hydrostatic equilibrium, the non-central part of the gravitational field described by equation (5), and resolved at the reference radius, has just two non-zero coefficients

$$J_2 = -C_{20} = \frac{5}{6} qk_{2f}$$
$$C_{22} = \frac{1}{4} qk_{2f} \qquad (16)$$

where we have followed the convention of expressing the zonal gravity coefficient according to $J_l = -C_{l0}$. For hydrostatic synchronous satellites, the ratio of the gravity coefficients is thus $J_2/C_{22} = 10/3$.

Likewise, if the body's shape is expressed in spherical harmonics as

$$H(\theta, \phi) = \sum_{l=0}^{\infty} \sum_{m=-l}^{l} H_{lm} Y_{lm}(\theta, \phi) \qquad (17)$$

where $H_{lm}$ are the degree-l and order-m spherical harmonic expansion coefficients representing the shape (with $H_{00} = R$), then the hydrostatic equilibrium figure is asymmetric in precisely the same way, with the coefficients

$$H_{20} = -\frac{5}{6} qRh_{2f}$$
$$H_{22} = \frac{1}{4} qRh_{2f} \qquad (18)$$

which, again, have the characteristic ratio $H_{20}/H_{22} = -10/3$. It is also common to describe the figure using the semiaxes ($a > b > c$) of an (approximately) equivalent triaxial ellipsoid, by evaluating equation (17) at the pole and at two points on the equator (at longitudes 0 and $\pi/2$), yielding

$$a = R \left( 1 + \frac{7}{6} qh_{2f} \right)$$
$$b = R \left( 1 - \frac{1}{3} qh_{2f} \right) \qquad (19)$$
$$c = R \left( 1 - \frac{5}{6} qh_{2f} \right)$$

This leads to another commonly referenced characteristic ratio for synchronous satellites in hydrostatic equilibrium

$$\frac{a-c}{b-c} = 4 \qquad (20)$$

The forgoing describes the condition of hydrostatic equilibrium in terms of both the expected equilibrium figure and the resulting asymmetries in the gravitational field. However, whereas the first-order approximation used to obtain equation (11) is adequate in most cases, and sufficient for a basic interpretation of the gravity data (e.g., *Iess et al.,* 2014), higher-order approximations become important for more precise modeling of fast rotating bodies like Enceladus (*Tricarico,* 2014; *McKinnon,* 2015), as we will discuss in section 2.3.

***2.1.5. Moments of inertia.*** In the previous section, we showed that, in the case of a body in perfect hydrostatic equilibrium, measuring either of the two degree-2 gravity coefficients, $J_2$ or $C_{22}$, is sufficient to recover the fluid Love number $k_{2f}$. This is very useful because $k_{2f}$ can be related to the body's moment of inertia using the Radau-Darwin equation (e.g., *Darwin,* 1899; *Murray and Dermott,* 1999)

$$\frac{C}{MR^2} = \frac{2}{3}\left(1 - \frac{2}{5}\sqrt{\frac{4 - k_{2f}}{1 + k_{2f}}}\right) \quad (21)$$

where C is the polar moment of inertia (i.e., about the spin pole, or c-axis).

The asymmetric nature of the tidally and rotationally deformed body means that its principal moments of inertia are not equal (see equation (3)). For a hydrostatic synchronous satellite, A < B < C; in the case of a non-synchronously rotating body, with no static tidal bulge, A = B < C.

It can be shown (e.g., *Hubbard,* 1984, p. 79) that the moment of inertia asymmetries are related to the degree-2 gravity coefficients according to

$$J_2 = \frac{C - \frac{1}{2}(A + B)}{MR^2}$$
$$C_{22} = \frac{B - A}{4MR^2} \quad (22)$$

from which it follows that the mean moment of inertia is

$$\frac{I}{MR^2} = \frac{C}{MR^2} - \frac{2}{3}J_2 \quad (23)$$

Having obtained the mean moment of inertia factor, we are finally in a position to constrain the internal density structure described by equations (1) and (2).

***2.1.6. Nonhydrostatic effects.*** An additional complication arises from the fact that solid planetary bodies, even large ones like Earth, have exteriors that are cold and rigid enough to support some non-hydrostatic topography, even over long timescales. In general, the measured shape and gravity are therefore a reflection of a mostly hydrostatic body, superimposed with some relatively smaller non-hydrostatic topography (and corresponding non-hydrostatic gravity). The challenge is that it is not necessarily obvious how to separate the hydrostatic and non-hydrostatic parts of these signals.

In previous work [e.g., Europa (*Anderson et al.,* 1998)], it was not possible to obtain independent constraints on $J_2$ and $C_{22}$ or to measure $H_{20}$ and $H_{22}$ with sufficient precision to confirm whether or not they conform to the hydrostatic expectation. Instead, the condition of hydrostatic equilibrium was assumed, allowing direct calculation of $k_{2f}$ from $C_{22}$ via equation (16), and yielding an estimate of the moment of inertia via equation (21). The Cassini mission, however, has enabled more precise and nearly independent measurements of each of these four quantities for the saturnian satellites Titan, Enceladus, Dione, and Rhea, and has revealed that the condition of hydrostatic equilibrium is generally not satisfied. For example, Titan's figure exhibits considerable excess flattening, with $-H_{20}/H_{22} = 4.9 \pm 0.1$ (*Zebker et al.,* 2012; *Hemingway et al.,* 2013a) in spite of its nearly hydrostatic gravity, for which $J_2/C_{22} = 3.32 \pm 0.02$ (*Iess et al.,* 2010, 2012). Similarly, Enceladus has considerable excess flatten-

ing, with $-H_{20}/H_{22} = 4.2 \pm 0.2$ (*Nimmo et al.,* 2011; *Thomas et al.,* 2016; *Tajeddine et al.,* 2017), while its gravity field is only modestly non-hydrostatic, with $J_2/C_{22} = 3.51 \pm 0.05$ (*Iess et al.,* 2014). For Dione, both the figure and gravity are considerably non-hydrostatic, with $-H_{20}/H_{22} = 5.2 \pm 0.6$ and $J_2/C_{22} = 4.00 \pm 0.06$ (*Thomas et al.,* 2007; *Nimmo et al.,* 2011; *Hemingway et al.,* 2016). While Rhea's shape is not as well determined, with $-H_{20}/H_{22} = 3.4 \pm 1.0$, its gravity field is substantially non-hydrostatic, with $J_2/C_{22} = 3.91 \pm 0.10$ (*Tortora et al.,* 2016).

This deviation from hydrostatic equilibrium complicates the interpretation, as we discuss below, but the combination of both shape and gravity observations allows some of the ambiguities to be resolved, and additionally provides information about how such unrelaxed topography is supported in the relatively stiff exterior. For example, the large non-hydrostatic topography and small non-hydrostatic gravity of Titan and Enceladus are suggestive of isostatic compensation (see section 2.3).

## 2.2. Observations

***2.2.1. Gravity determination.*** Cassini carried out gravity measurements of Enceladus during three flybys on April 28, 2010; November 30, 2010; and May 2, 2012 (labeled as E9, E12, and E19). Flyby altitude and latitude were selected to enhance the signature of a hemispherical asymmetry of the gravity field, characterized mainly by the harmonic coefficient $J_3$. E9 and E19 occurred over the south polar region (latitude 89°S and 72°S), at closest approach altitudes of 100 and 70 km, respectively. E12 was over the north polar region (latitude 62°N), at an altitude of just 48 km. The small closest approach distances were required by the need to maximize the spacecraft accelerations due to Enceladus' gravity field.

The estimation of the mass and gravity field was obtained solely from measurements of the spacecraft range rate (Doppler). Range rate is approximately equal to twice the line-of-sight projection of the spacecraft velocity with respect to a ground antenna. This observable quantity is a standard product of the radio tracking system and is crucial for the accurate navigation of the spacecraft. Although other radiometric data are used for orbit reconstruction (such as range), range rate is by far the most valuable for geodesy applications. The range rate of Cassini is measured at a ground antenna of NASA's Deep Space Network (DSN) after establishing a coherent, two-way, microwave link at X-band (7.2–8.4 GHz). In this configuration, the ground antenna transmits a radio signal (a monochromatic carrier, possibly modulated for telecommands and ranging) generated by a highly stable frequency reference. The signal is then received onboard by means of a transponder, then coherently retransmitted back to Earth. The frequency of the beat tone between the incoming and the outgoing signal provides the Doppler shift and the (two-way) range rate.

The Cassini X-band radio system delivers measurement accuracies up to 0.01 mm s$^{-1}$ at 60-s integration times un-

der favorable conditions (although 2–4 times higher noise is more frequently encountered). On timescales relevant to Cassini gravity investigations, the noise is dominated by path delay variations due to interplanetary plasma and tropospheric water vapor. During the three gravity flybys of Enceladus, the (two-way) range rate noise was 0.017 mm s$^{-1}$ (E9), 0.027 mm s$^{-1}$ (E12), and 0.036 mm s$^{-1}$ (E19) at 60 s integration time.

The estimation of Enceladus's gravity field with Cassini poses several challenges, all traceable to three factors. First, the small number of flybys strongly limits the sampling of the gravity field and does not permit breaking the correlations between some estimated parameters. Second, the spacecraft acceleration due to the moon's gravity is quite small (surface gravity is only ~0.11 m s$^{-2}$), and so is the change in the spacecraft range rate measured by the ground antenna. Third, the gravitational interaction time of the spacecraft with the small moon is short.

The velocity variation induced by the monopole gravity, and the zonal harmonics of degree 2 and 3 can be computed from elementary arguments. Neglecting factors on the order of unity, we simply multiply the acceleration due to each harmonic by the interaction time r/V (r being the Cassini-Enceladus distance and V the nearly constant relative velocity) and obtain

$$dV^{(0)} \approx \frac{GM}{rV}$$

$$dV^{(2)} \approx \frac{GM}{rV}\left(\frac{R}{r}\right)^2 J_2 \qquad (24)$$

$$dV^{(3)} \approx \frac{GM}{rV}\left(\frac{R}{r}\right)^3 J_3$$

Here, GM is the gravitational parameter of Enceladus and R is the reference radius (252.1 km). Note that, for close flybys (r–R ≪ R), the velocity variation scales with the product $\rho R^2$, where $\rho$ is the mean density. Using the values reported by *Iess et al.* (2014), the velocity changes due to GM, $J_2$, and $J_3$ are, respectively, about 3–4 m s$^{-1}$, 1.1–1.4 cm s$^{-1}$, and 0.2–0.3 mm s$^{-1}$. Although all these values are well above the noise threshold of the Cassini radio system, the various contributions are not fully separable with only three flybys.

Gravity and orbits of the spacecraft and Enceladus were recovered by fitting the range rate data using orbit determination software developed at JPL for deep space navigation. These tools (ODP and the recently developed MONTE) generate computed observables using a fully relativistic model of the spacecraft dynamics and radio signal propagation. The residuals (observed range rate minus computed range rate) are minimized through an iterative process where a set of free parameters is adjusted by linearizing the observation equations. The output of the process is a set of estimated parameters and their covariances. The estimated parameters included the full satellite degree-2 harmonic coefficients, $J_3$, the position and velocity of Cassini at each flyby, and corrections to the mass and the orbital elements of Enceladus. In

the nominal solution, the tesseral and sectorial components of the degree-3 field were assumed to be zero. This set of parameters was the minimum set able to fit the data. As a test of the stability of the model, an alternate solution, which also estimated the remaining degree-3 terms, was obtained. The result is statistically identical to the nominal result, although the uncertainties increase. All the additional degree-3 terms are compatible with zero within 2σ or less, and thereby add no new information (*Iess et al.,* 2014, section S2.1). The non-gravitational accelerations due to the anisotropic thermal emission from Cassini's radioisotope thermoelectric generators and the solar radiation pressure were accounted for using previous estimates obtained during the saturnian tour. The associated uncertainties were considered in the construction of the covariance matrix.

A good orbital fit would not be possible without also including the small but non-negligible aerodynamic drag experienced by Cassini when it flew through the plumes in the southern polar flybys E9 and E19. The dynamical effect was modeled as a nearly impulsive, vectorial acceleration at closest approach, to be estimated together with the other parameters. An equivalent method relies on models of the neutral particle density and estimates the aerodynamic coefficient of the spacecraft. Both methods lead to statistically identical solutions for the gravity field. The estimated, aerodynamic $\Delta V$ is almost parallel to the spacecraft velocity V (as expected for a drag force), with a magnitude of 0.25 mm s$^{-1}$ for E9 and 0.26 mm s$^{-1}$ for E19. The $\Delta V$ experienced by Cassini is comparable to the effect of the $J_3$ harmonic.

As expected, the gravity field is dominated by the $J_2$ and $C_{22}$ harmonics, associated with the rotational and tidal deformation of Enceladus (Table 1). The estimate of $J_2$ and $C_{22}$ is quite precise (about 1%, 1σ). $C_{2,1}$, $C_{2,-1}$, and $C_{2,-2}$ are consistent with a null value at the 2σ level. $C_{2,2}$ is about one order of magnitude larger than $J_3$, which is estimated to a relative accuracy of about 20%. The positive sign of $J_3$ implies a negative mass anomaly at the south pole (consistent with the observed topography), but its small value indicates the presence of a compensating positive mass anomaly at depth (see section 2.3).

***2.2.2. Shape determination.*** The shape of Enceladus has been determined based on analysis of limb profiles collected over the course of the Cassini mission (*Thomas et al.,* 2007;

TABLE 1. Gravity model (*Iess et al.,* 2014) (unnormalized, dimensionless potential coefficients, for $R_{ref}$ = 252.1 km).

| Parameter | Value ±1σ |
|---|---|
| GM | 7.210443 ± 0.00003 km$^3$ s$^{-2}$ |
| $J_2 = -C_{2,0}$ | 5526.1 ± 35.5 × 10$^{-6}$ |
| $C_{2,1}$ | 9.4 ± 11.8 × 10$^{-6}$ |
| $C_{2,-1}$ | 40.5 ± 22.8 × 10$^{-6}$ |
| $C_{2,2}$ | 1575.7 ± 15.9 × 10$^{-6}$ |
| $C_{2,-2}$ | 23.0 ± 7.5 × 10$^{-6}$ |
| $J_3 = -C_{3,0}$ | −118.2 ± 23.5 × 10$^{-6}$ |
| $J_2/C_{2,2}$ | 3.51 ± 0.05 |

*Thomas,* 2010; *Nimmo et al.,* 2011; *Tajeddine et al.,* 2017). The best fitting triaxial ellipsoidal figure exhibits substantial polar flattening, with $a–c \approx 8.5$ km and a significant departure from hydrostatic equilibrium, with $(a–c)/(b–c) \approx 2.8$ (recall that the hydrostatic ratio is 4). Similarly, in terms of spherical harmonic coefficients, the ratio of the degree-2 zonal to sectorial terms is ~4.2, much higher than the ~3.3 expected if Enceladus were in hydrostatic equilibrium (Table 2). The limb profiles provide sufficient spatial coverage to constrain global spherical harmonic models up to degree and order 8 (*Nimmo et al.,* 2011); the recent addition of stereogrammetric measurements has extended the latest topography models to degree and order 16 (*Tajeddine et al.,* 2017). One of the most significant features of the shape is the topographic depression associated with the SPT, having an elevation that is ~1.1 km lower than at the north pole, an effect that is expressed mainly in the $H_{30}$ term (Table 2).

TABLE 2.  Shape model (*Nimmo et al.,* 2011) (unnormalized).

| Parameter | Value $\pm 1\sigma$ |
|---|---|
| R | 252.1 km |
| $H_{2,0}$ | $-3846 \pm 179$ m |
| $H_{2,1}$ | $0 \pm 52$ m |
| $H_{2,-1}$ | $-65 \pm 52$ m |
| $H_{2,2}$ | $917 \pm 19$ m |
| $H_{2,-2}$ | $-39 \pm 19$ m |
| $H_{3,0}$ | $384 \pm 5$ m |
| $-H_{2,0}/H_{2,2}$ | $4.20 \pm 0.22$ |

## 2.3.  Modeling and Interpretation

*2.3.1.  Basic interpretation.*  Since the gravity field of Enceladus was first measured (*Iess et al.,* 2014), its interpretation has been an active area of research (*Iess et al.,* 2014; *McKinnon,* 2015; *Čadek et al.,* 2016, 2017; *van Hoolst et al.,* 2016; *Beuthe et al.,* 2016; *Hemingway and Mittal,* 2017). In part because of Enceladus' small size and rapid rotation rate, interpretation of the data is unusually sensitive to modeling details, as we discuss below. Nevertheless, there are a few basic observations that are uncontroversial.

The first is that while the shape is substantially non-hydrostatic, with $H_{20}/H_{22} = -4.20 \pm 0.22$ ($1\sigma$), the gravity field is only modestly so, with $J_2/C_{22} = 3.51 \pm 0.05$ ($1\sigma$). This situation is immediately suggestive of compensation. Without compensation, the large non-hydrostatic topography should give rise to a correspondingly large non-hydrostatic gravity signal. Likewise, the observed $J_3$ gravity anomaly, $(-118 \pm 23) \times 10^{-6}$, is substantially smaller than would be expected if the ~1-km north-south polar elevation difference were completely uncompensated ($\approx -375 \times 10^{-6}$).

A compensation mechanism is therefore required. Although there are several possibilities, including systematic lateral variations in density (i.e., Pratt isostasy) or non-hydrostatic topography on the surface of the rocky core (see section 2.3.5), the most straightforward mechanism, which

naturally yields a small non-hydrostatic gravity signal in spite of the large non-hydrostatic topography, is Airy-type isostatic compensation. That is, Enceladus' long wavelength topography appears to be supported, at least in part, by the displacement of a relatively low viscosity, higher density material beneath the crust — e.g., a subsurface liquid ocean.

*2.3.2.  Admittance analysis.*  The presence of non-hydrostatic degree-2 gravity and topography prevents direct calculation of the moment of inertia via equations (16) and (21). Instead, it is necessary to first separate the observed degree-2 gravity and topography signals into their hydrostatic and non-hydrostatic parts (*Iess et al.,* 2014). Assuming these components can be separated linearly (a reasonable assumption as long as the non-hydrostatic parts are small compared to the hydrostatic parts), we can write

$$
\begin{aligned}
J_2^{obs} &= J_2^{hyd} + J_2^{nh} \\
C_{22}^{obs} &= C_{22}^{hyd} + C_{22}^{nh} \\
H_{20}^{obs} &= H_{20}^{hyd} + H_{20}^{nh} \\
H_{22}^{obs} &= H_{22}^{hyd} + H_{22}^{nh}
\end{aligned}
\tag{25}
$$

where the superscripts refer to the observations (obs), the hydrostatic expectation (hyd) given by equations (16) and (18), and the non-hydrostatic components (nh). For a given assumed moment of inertia, the only unknowns in equation (25) are the non-hydrostatic components. The relationship between these non-hydrostatic gravity and topography signals can be quantified by the ratios

$$
\begin{aligned}
Z_{20} &= -J_2^{nh}/H_{20}^{nh} \\
Z_{22} &= C_{22}^{nh}/H_{22}^{nh}
\end{aligned}
\tag{26}
$$

This is effectively a component-wise version of the spectral admittance (e.g., *Wieczorek,* 2015), a quantity related to the degree and depth of isostatic compensation:  Greater and/or shallower compensation results in a more muted gravity signal and thus a smaller admittance. The advantage of this approach is that, provided the ice shell's mechanical properties are not significantly variable laterally, we should expect that $Z_{20} = Z_{22}$. Hence, we obtain self-consistent results when we find a moment of inertia that, via equations (21), (16), (18), (25), and (26), yields $Z_{20} = Z_{22}$.

It is worth emphasizing, however, that, for a body like Enceladus, the expectation that $Z_{20} = Z_{22}$ is an assumption that has not been explicitly tested in the literature to date. Future work to better justify this assumption, or to investigate the effect of relaxing it to some degree, may be valuable.

Considering a wide range of possible mean moments of inertia, *Iess et al.* (2014) produced the equivalent of Fig. 2a. This result follows from the first-order equilibrium figure theory described by equation (11) — an approximation that becomes increasingly poor for fast-rotating bodies like Enceladus (*Tricarico,* 2014). To account for this effect, *McKinnon* (2015) repeated the analysis of *Iess et al.* (2014) using a fourth-order theory of figures approach (*Tricarico,* 2014), yielding instead the equivalent of Fig. 2b. Whereas

the first-order results indicate a preferred admittance of $Z_2 \approx 11.8 \pm 1.6$ mGal km$^{-1}$ and a mean moment of inertia factor of $\sim 0.333 \pm 0.002$, the fourth-order results suggest instead $Z_2 \approx 15.7 \pm 2.0$ mGal km$^{-1}$ and $\sim 0.331 \pm 0.002$. While the difference may appear subtle, the implications for compensation depth (and hence ice shell thickness) are significant.
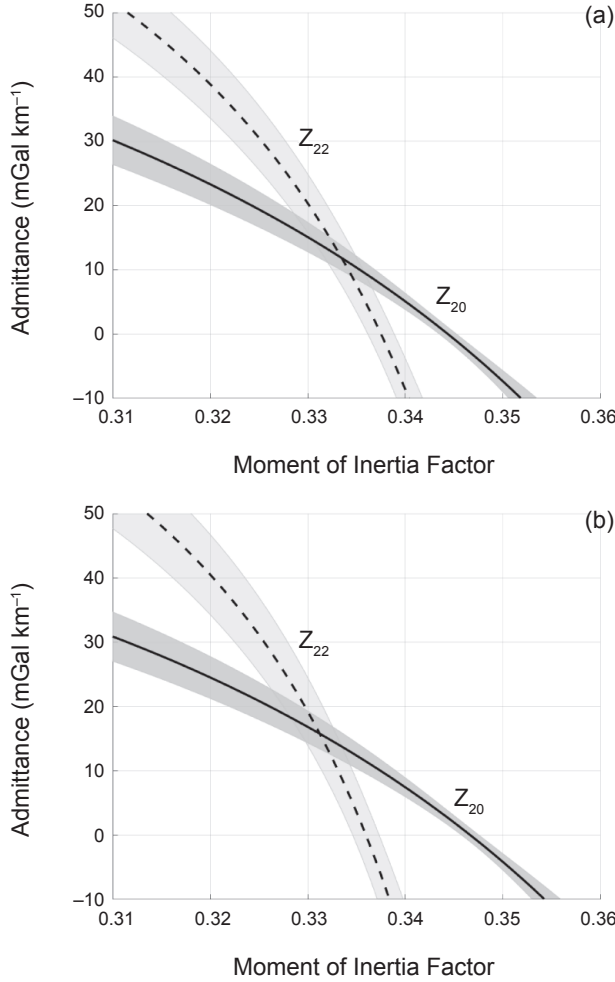


**Fig. 2.** Comparison of degree-2 zonal ($Z_{20}$, solid line) and sectorial ($Z_{22}$, dashed line) admittances across a range of possible mean moments of inertia. Shaded bands indicate 1$\sigma$ uncertainties propagated from both the shape and gravity models. The point of intersection represents the admittance and moment of inertia combination that yields self-consistent results. **(a)** Replication of the *Iess et al.* (2014) results, following from first-order equilibrium figure theory (except using gravity coefficients from Table 1). **(b)** Replication of *McKinnon* (2015) results, employing fourth-order methods of *Tricarico* (2014). Unlike in *Iess et al.* (2014) and *McKinnon* (2015), admittances are here given in the more commonly used units of mGal km$^{-1}$ (where 1 mGal = 10$^{-5}$ m s$^{-2}$), obtained by converting the dimensionless gravitational potential coefficients in equation (26) to acceleration by multiplying them by $(l+1)GM/R^2$.

In addition to the degree-2 signals, the zonal terms of the degree-3 gravity and topography are available and can be used to obtain the zonal part of the degree-3 admittance, $Z_{30} \approx 14.0 \pm 2.8$ mGal km$^{-1}$. The degree-3 observations provide an independent admittance estimate that also has the advantage of not being complicated by tidal and rotational deformation (the theoretical hydrostatic equilibrium figure has no degree-3 components), and is therefore independent of moment of inertia.

To put these admittance values in context, assuming a density of $\rho_c = 925$ kg m$^{-3}$ for the icy crust, the degree-2 and -3 admittances expected in the case of zero compensation are $Z_2 \approx 47$ mGal km$^{-1}$ and $Z_3 \approx 44$ mGal km$^{-1}$. The fact that the observed admittances are much smaller is another indication that the topography is significantly compensated. Although the degree-2 admittance values depend on the assumed mean moment of inertia, even without requiring that $Z_{20} = Z_{22}$, the small values of both $Z_{20}$ and $Z_{22}$ suggest compensation independently. Although $Z_{22}$ becomes compatible with uncompensated topography for moments of inertia below $\sim 0.32$, this seems unlikely, as it would require Enceladus to be one of the most strongly differentiated solid bodies in the solar system. This observation also provides a clue about the spatial extent of the subsurface liquid layer (assuming Airy type compensation): Whereas a south polar regional sea could account for the smallness of the zonal admittance terms ($Z_{20}$ and $Z_{30}$), the small value of $Z_{22}$ requires a more extensive, perhaps global, subsurface liquid layer.

*2.3.3. Compensation model.* Further interpretation of the admittance values requires a compensation model. While most authors to date have favored Airy isostasy to explain the compensation of Enceladus' long wavelength topography (*Iess et al.,* 2014; *McKinnon,* 2015; *Čadek et al.,* 2016; *Beuthe et al.,* 2016; *Hemingway and Mittal,* 2017), there are multiple ways to conceive of Airy compensation, leading to subtle but consequential differences between the models and their implications. Moreover, the introduction of elastic stresses to the models widens the parameter space considerably, and can have a significant effect on the results — an issue we discuss further below.

The non-hydrostatic topography gives rise to non-hydrostatic gravitational acceleration according to (*Jeffreys,* 1976; *Burša and Peč,* 1993)

$$g_{lm}(R) = \frac{l+1}{2l+1} 4\pi G \sum_i \Delta\rho_i H_{ilm} \left(\frac{R_i}{R}\right)^{l+2} \quad (27)$$

where R is the body's mean radius, G is the gravitational constant, $H_{ilm}$ describes the degree-l and order-m non-hydrostatic topography at the top of the $i^{th}$ layer, whose mean outer radius is $R_i$, and where $\Delta\rho_i$ is the density contrast between the $i^{th}$ layer and the layer above it.

Assuming Airy compensation, and ignoring the role of elastic support for the moment, the relief at the base of the ice shell mirrors the non-hydrostatic surface relief with the amplitude scaled by $\rho_c/\Delta\rho$, where $\rho_c$ is the density of the crust (or ice shell) and $\Delta\rho$ is the density contrast between

the ice shell and the underlying ocean. In this case, the non-hydrostatic topography at the top (t) and bottom (b) of the crust are related by

$$H_{blm} = -H_{tlm} \frac{\rho_c}{\Delta\rho} \gamma \qquad (28)$$

Here, the dimensionless factor $\gamma$ is a placeholder allowing for various conceptions of Airy isostasy and different types of elastic support, as discussed below.

In general, the model admittance (gravity/topography ratio) can thus be written

$$Z(1) = \frac{1+1}{2l+1} 4\pi G\rho_c \left( 1 - \gamma \left( \frac{R_b}{R_t} \right)^{1+2} \right) \qquad (29)$$

where $R_t$ and $R_b$ are the radii corresponding to the top and bottom of the ice shell, respectively (the mean shell thickness being d = $R_t$–$R_b$).

Equations (27) and (29) implicitly treat the non-hydrostatic topography as a surface density anomaly — an approximation that is good when the topography is sufficiently small. In the present case, however, the small density contrast between the ice shell and the ocean leads to substantial relief at the ice/ocean interface. Taking this finite-amplitude into account (e.g., *Martinec,* 1994; *Wieczorek and Phillips,* 1998), one obtains a slightly smaller admittance. Although we neglect this effect in our discussion here, within the context of any particular compensation model, the effect can be significant, and so some authors do take it into account (e.g., *Čadek et al.,* 2016; *Hemingway and Mittal,* 2017).

In the limit of zero elastic support, and when isostasy is defined as requiring equal masses in columns of equal solid angle, then $\gamma = (R_t/R_b)^2$ (e.g., *Wieczorek,* 2015); the requirement of equal pressures at equal depths instead leads to $\gamma = (g_t/g_b)$, where $g_t$ and $g_b$ are the mean gravitational acceleration at the top and bottom of the ice shell, respectively (*Hemingway and Matsuyama,* 2017); when the total weight of the surface topography is required to equal the buoyancy force of the basal relief, then $\gamma = (g_t/g_b)(R_t/R_b)^2$ (e.g., *Čadek et al.,* 2016). Unfortunately, these different definitions of isostasy lead to significantly different estimates of the compensation depth.

Assuming a crustal density of $\rho_c$ = 925 kg m$^{-3}$, the observed degree-3 admittance suggests a compensation depth of between 18 km and 30 km, depending on how one defines isostasy [the "equal masses" model leads to the largest compensation depth estimate; the "equal pressures" model leads to the smallest (*Hemingway and Matsuyama,* 2017)], in agreement with the result following from the degree-2 admittance obtained using first-order equilibrium figure theory (*Iess et al.,* 2014). The degree-2 admittance obtained using fourth-order equilibrium figure theory (*Tricarico,* 2014; *McKinnon,* 2015) instead suggests a compensation depth of between 24 km and 47 km, again, depending on how isostasy is defined. Accounting for uncertainties in the observed shape and gravity, the range of possible compensa-

tion depths expands even further: from ~14 km at the low end of the estimated degree-3 admittance to ~53 km at the high end of the estimated degree-2 admittance.

When elastic support is included, $\gamma$ decreases in the case of surface loading (e.g., due to impacts or sedimentation/erosion at the surface) and increases in the case of basal loading (e.g., freezing/melting/relaxation at the base of the crust), and can have a significant effect on the resulting compensation depth estimate (*Hemingway and Mittal,* 2017). For instance, adding even an effective 200-m elastic layer can decrease the estimated compensation depth by more than a factor of 2 (*Čadek et al.,* 2016), assuming the shell thickness variations are generated at the surface; the compensation depth estimate increases if the shell thickness variations are instead generated at the base of the shell (*Beuthe et al.,* 2016; *Hemingway and Mittal,* 2017).

Further details of elastic/viscoelastic support models are beyond the scope of this chapter, but it should be noted that this remains an active area of research (*Čadek et al.,* 2016; *Soucek et al.,* 2016; *Hemingway and Mittal,* 2017). In particular, it is not yet clear how elastic support of the long-wavelength topography is affected by factors such as lateral variations in the shell's elastic properties (*Beuthe,* 2008; *Čadek et al.,* 2016, 2017), or the way bending and membrane stresses are transmitted across the SPT given the presence of the major fracture systems (i.e., the Tiger Stripes) in that region (e.g., *Soucek et al.,* 2016).

Although the range of possible mean ice shell thicknesses (i.e., mean compensation depths) can be narrowed by arguing for one or another compensation model, researchers have yet to converge on the best approach, making it difficult to make definitive statements about the ice shell thickness. However, assuming some version of Airy compensation, a few things can be stated with confidence. First, the thinnest part of the ice shell must be located beneath the large topographic depression at the south pole. Since the shell thickness is necessarily greater than zero there, this provides an effective lower bound on the mean shell thickness. Depending on the definition of isostasy, and the assumed ice shell and ocean densities, one finds that the mean shell thickness must be at least ~18 km in order to ensure nonzero shell thickness at the south pole. An upper bound on the shell thickness is harder to establish. However, as long as the degree-3 observations are taken into account, the mean shell thickness is unlikely to exceed ~44 km. Shell thicknesses greater than 44 km would lead to degree-3 admittances more than 2$\sigma$ larger than the observed value, even when using the isostasy model that produces the smallest admittances [i.e., the "equal masses" model, with $\gamma = (R_t/R_b)^2$]. Again, however, the possibility of substantial elastic support of basal topography can allow for larger mean shell thicknesses.

***2.3.4. Internal structure.*** The simplest approach to modeling the internal density structure is to start by assuming a two-layer body. If the density of the outer H$_2$O layer (ocean plus ice shell) is prescribed, then with the known bulk density (1609 kg m$^{-3}$) and the moment of inertia obtained from the admittance analysis, we can use equations (1) and (2) to

solve for the core radius and density (Fig. 3). A mean core radius of ~192 km leaves ~60 km for the mean thickness of the H₂O layer. If the mean compensation depth (i.e., ice shell thickness) is ~30 km, this leaves a mean ocean thickness of ~30 km, neglecting the effect of the small difference in densities between the ice shell and the ocean (*Iess et al.,* 2014; *McKinnon,* 2015). More sophisticated three-layer models have also been constructed (*Čadek et al.,* 2016; *Hemingway and Mittal,* 2017), yielding broadly similar results (Table 3).

A few basic conclusions emerge immediately. First, the low density of the (presumably silicate) core suggests hydrothermal alteration (e.g., serpentinization) and/or substantial porosity, which may be easy to maintain given the modest internal pressures (Fig. 4). In particular, an unconsolidated rubble pile core, with water-filled pores, is possible (*Roberts,* 2015). The combined thickness of the H₂O layers is reasonably well constrained, but the models permit some tradeoff between the thicknesses of the ice shell and the ocean (e.g., *Hemingway and Mittal,* 2017). Although these tradeoffs have little effect on the density and therefore the internal pressure and gravity profiles (Fig. 4), they do make it difficult to determine the shell thickness with precision. This is regrettable since the thickness of the ice shell has a number of important implications. We discuss the ice shell's possible structure, dynamics, and related implications in section 4.

**2.3.5. Additional considerations.** In the models discussed so far, the core shape has been assumed to conform to an equipotential, as expected if the core shape was established when the interior was warm. The small internal gravity and pressure, however, means that the surface of the core could, in principle, support considerable non-hydrostatic topography over long timescales. Indeed, an irregular core shape had previously been proposed to account for the non-hydrostatic shape of Enceladus' surface (*Thomas et al.,* 2007; *McKinnon,* 2013) and to explain the rotation state of the similarly sized Mimas (*Tajeddine et al.,* 2014). However, while the presence of non-hydrostatic core topography would contribute to the observed gravity, there is no reason to expect it to do so in precisely such a way as to offset the gravity anomalies associated with the surface topography. That is, there is no reason to expect the non-hydrostatic core topography to effectively mirror the non-hydrostatic surface topography, as would be required for it to be substantially responsible for the compensating effect observed in the gravity data. In fact, it is just as likely, if not more so, that non-hydrostatic core topography would have the opposite effect, as would be expected in the case of an overly oblate or tidally elongated core. While the core shape may not be precisely hydrostatic, the hydrostatic assumption may be justified on the grounds that it is the most parsimonious. Although it has not been done in the literature to date, some unknown non-hydrostatic core topography could be added as a free parameter, and would increase uncertainties in the other estimated parameters.

Whereas all the models discussed so far assume some version of Airy-type isostasy, in which the surface topography is supported in part by lateral variations in the ice shell's thickness, it should be noted that the topography could also be supported in part by lateral variations in density [i.e., Pratt-type isostasy (e.g., *Besserer et al.,* 2013; *Tajeddine et al.,* 2017)]. This mechanism is unlikely to be primarily responsible for the observed compensation, however, because it would require parts of the heavily cratered plains to exhibit a higher crustal density, which is the opposite of what one would expect (e.g., *McKinnon,* 2015; *Hemingway and Mittal,* 2017) and because it would require the density variations to extend through an unrealistically large depth of ~40 km (*Hemingway and Mittal,* 2017). Nevertheless, the potential compensating effect of lateral variations in density cannot be ruled out entirely.
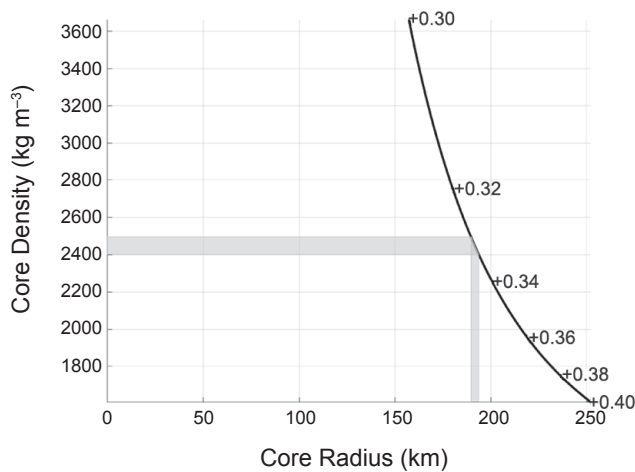


**Fig. 3.** Core radius and density over a range of possible mean moments of inertia (I/MR² = 0.30–0.40), assuming a two-layer body with outer layer density fixed at ρ = 950 kg m⁻³. The estimated mean moment of inertia (0.331 ± 0.002) corresponds to a core radius of ~192 km and a core density of ~2450 kg m⁻³.
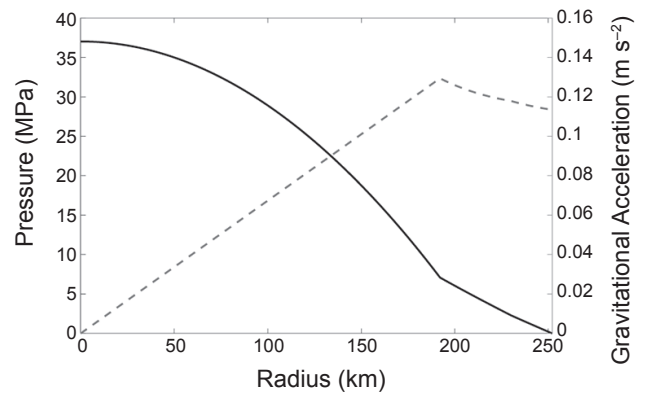


**Fig. 4.** Interior pressure (solid line) and gravity (dashed line) profiles for a three-layer model of Enceladus with 22-km mean thickness ice shell (900 kg m⁻³), 38-km mean thickness ocean (1030 kg m⁻³), and 192-km radius core (~2450 kg m⁻³).

TABLE 3.  Comparison of published interior models.

| Model | Core | Ocean | Ice Shell | Notes |
|---|---|---|---|---|
| *Iess et al.* (2014) | ~190 km (~2400 kg m$^{-3}$) | 10–30 km (1000 kg m$^{-3}$*) | 30–40 km (920 kg m$^{-3}$*) | *Based on gravity and topography:* Hydrostatic terms from first-order equilibrium figure theory; elastic support deemed insignificant; both regional and global oceans discussed, but left as an open question. |
| *McKinnon* (2015) | 190–195 km (~2450 kg m$^{-3}$) | ~10 km (1007 kg m$^{-3}$*) | ~50 km (925 kg m$^{-3}$*) | *Based on gravity and topography:* Hydrostatic terms from fourth-order equilibrium figure theory (*Tricarico,* 2014); elastic support deemed insignificant; ice shell thickness determination is based on degree-2 data only (degree-3 data deemed to have only regional significance). |
| *Thomas et al.* (2016) | ~200 km (~2300 kg m$^{-3}$) | 26–31 km (1000 kg m$^{-3}$*) | 21–26 km (~850 kg m$^{-3}$) | *Based on physical libration amplitude:* Three-layer model with layer interfaces assumed to be hydrostatic and defined by first-order equilibrium figure theory; ice shell thickness constrained by libration amplitude. Core and ice shell densities adjusted to fit the moment of inertia reported by *Iess et al.* [2014]. |
| *Čadek et al.* (2016) | 180–185 km (~2450 kg m$^{-3}$) | ~50 km (~1030 kg m$^{-3}$) | 18–22 km (925 kg m$^{-3}$*) | *Based on gravity, topography, and librations:* Elastic support (assuming top loading) introduced in order to bring gravity-based shell thickness estimate into agreement with *Thomas et al.* (2016); Airy compensation model modified to account for radial variation in gravity; finite-amplitude correction included (*Martinec,* 1994). |
| *Van Hoolst et al.* (2016) | 170–205 km (2158–2829 kg m$^{-3}$) | 21–67 km (950–1100 kg m$^{-3}$) | 14–26 km (900–1000 kg m$^{-3}$) | *Based on physical libration amplitude:* Similar to *Thomas et al.* (2016) but additionally accounting for uncertainties on libration amplitude arising from rigidity and viscoelastic behavior of the ice shell, a wider range of ice and ocean densities, and the possibility of core topography; relaxes assumption of Airy compensation. |
| *Beuthe et al.* (2016) | 186–196 km (2350–2480 kg m$^{-3}$) | 34–42 km (1020 kg m$^{-3}$*) | 19–27 km (925 kg m$^{-3}$*) | *Based on gravity and topography:* Three-layer model with hydrostatic terms from second-order equilibrium figure theory (*Zharkov,* 2004); isostatic compensation achieved by minimizing deviatoric stresses (e.g., *Dahlen,* 1982). |
| *Hemingway and Mittal* (2017) | 188–205 km (2200–2450 kg m$^{-3}$) | 12–36 km (1000–1100 kg m$^{-3}$) | 22–41 km (850–950 kg m$^{-3}$) | *Based on gravity and topography:* Three-layer model with equilibrium figures determined numerically (*Tricarico,* 2014); Airy compensation model modified to ensure equal pressures at depth (*Hemingway and Matsuyama,* 2017); using newer shape model (*Tajeddine et al.,* 2017); finite-amplitude correction included (*Wieczorek and Phillips,* 1998). |

*Values that were prescribed rather than derived.

Thicknesses refer to mean layer thickness; lateral thickness variations are required by all models.

## 3. IMPLICATIONS FROM LIBRATIONS

In the previous section, we saw how tidal and rotational forces deform synchronous satellites like Enceladus into approximately triaxial ellipsoidal figures. We discussed how the resulting asymmetries in the mass distribution lead to differences among the principal moments of inertia, how these moments of inertia are related to observable asymmetries in the gravitational field, and how the moments of inertia are related to the satellite's internal structure. Here we look at how a satellite's rotational dynamics depend on the principal moments of inertia, focusing specifically on how the amplitude of forced physical librations can help to constrain the interior structure.

Most satellites in the solar system are locked in a 1:1 spin:orbit resonance, where the satellite's mean rotation rate is equal to its orbital mean motion. In this configuration, and assuming a circular orbit, the long axis of the satellite (i.e., its static tidal bulge) always points toward the parent body (the central planet). The eccentricity of the satellite's orbit, however, causes it to move faster at pericenter and slower at apocenter, even as the rotation rate remains (nearly) constant, leading to misalignments between the satellite's long axis and the line connecting the two bodies. To a first approximation, the long axis of the satellite points at the empty focus of the satellite's elliptical orbit (*Murray and Dermott,* 1999, p. 44). In a frame fixed on the planet, the satellite thus appears to rock back and forth about its spin axis as it orbits the planet — these apparent oscillations, called "optical librations," explain in part why more than 50% of the nearside of the Moon is visible from Earth.

Because of the periodic misalignments between the satellite's long axis and the satellite-planet line, the planet exerts gravitational torques on the satellite's static tidal bulge, creating additional oscillations called "physical longitudinal librations." Whereas the amplitude of the optical libration depends only on the orbital eccentricity, the physical libration amplitude additionally depends on the satellite's moments of inertia, thus making its measurement a valuable tool for constraining the internal structure [e.g., for the Moon (*Dickey et al.,* 1994), Mercury (*Margot et al.,* 2007), Phobos (*Willner et al.,* 2010; *Nadezhdina and Zubarev,* 2014), Janus and Epimetheus (*Tiscareno et al.,* 2009), Mimas (*Tajeddine et al.,* 2014), and Enceladus (*Thomas et al.,* 2016)].

### 3.1. Theory

The rotation of a satellite orbiting a central planet with mass m is described by the three Euler equations of motion (*Danby,* 1988; *Murray and Dermott,* 1999)

$$A\dot{\omega}_x - (B-C)\omega_y\omega_z = 3Gm(C-B)YZ/r^5$$
$$B\dot{\omega}_y - (C-A)\omega_z\omega_x = 3Gm(A-C)ZX/r^5 \qquad (30)$$
$$C\dot{\omega}_z - (A-B)\omega_x\omega_y = 3Gm(B-A)XY/r^5$$

where A, B, and C are the satellite's principal moments of inertia; $\omega_x$, $\omega_y$, and $\omega_z$ are the projections of the spin vector onto the satellite's principal axes, x, y, and z; X, Y, and Z represent the coordinates of the planet in the satellite's principal frame; and r is the distance between the satellite and the planet.

When the satellite's obliquity is negligible (i.e., when its spin pole is normal to its orbital plane), then $\omega_x = \omega_y = 0$, and the problem is reduced to two dimensions (Fig. 5). The small obliquity expected for Enceladus (*Chen and Nimmo,* 2011; *Baland et al.,* 2016) makes this a reasonable approximation for purposes of our discussion.

If we define $\psi$ as the angle between the satellite's long axis and the line connecting the two bodies, then we have $X/r = \cos\psi$ and $Y/r = \sin\psi$, which reduces the third line in equation (30) to

$$\ddot{\theta} = \frac{3}{2}\frac{(B-A)}{C}\frac{Gm}{r^3}\sin 2\psi \qquad (31)$$

where we now use $\ddot{\theta}$ to represent the variation in the satellite's angular velocity. Here, $\theta$ is the orientation of the satellite's long axis with respect to a fixed inertial reference frame
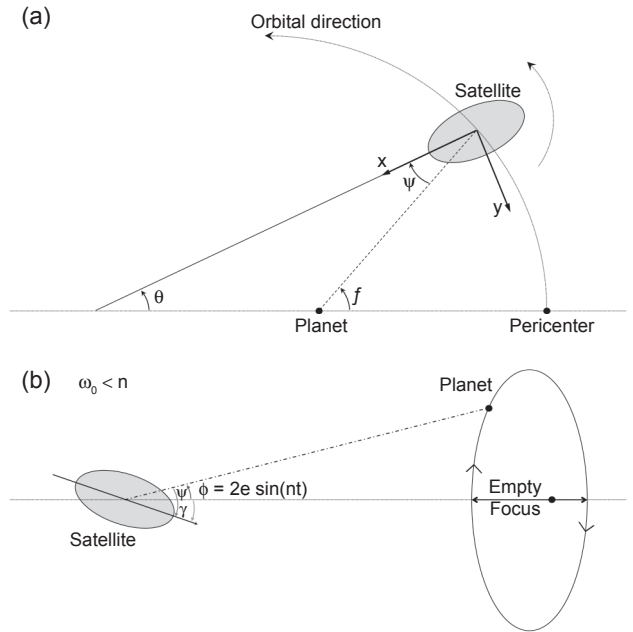


**Fig. 5.** The geometry of a satellite subject to librations illustrated **(a)** in a frame fixed on the planet; and **(b)** in a frame fixed on the satellite and oriented with the x-axis pointing toward the empty focus of the satellite's orbit. In **(a)**, f represents the true anomaly for the satellite, while $\theta$ represents the orientation of its long axis with respect to a fixed inertial frame. In **(b)**, $\phi$ represents the angle between the satellite-planet line and the line connecting the satellite with the empty focus of its orbit [this is the optical libration angle, not shown in **(a)**]; $\gamma$ is the physical libration. After *Tiscareno et al.* (2009).

(where $\theta = 0$ corresponds to pericenter). This variation in angular velocity goes as (B–A)/C because the longitudinal torques the planet exerts on the satellite are proportional to the satellite's moment of inertia difference, B–A, and because the polar moment of inertia, C, represents the resistance to those torques.

We also define $\phi$ to be the angle between the line connecting the two bodies and the line connecting the satellite with the empty focus of its orbit (Fig. 5b) — this is the optical libration angle. In the absence of longitudinal torques, the satellite's long axis would remain pointed at the empty focus, so that $\psi$ would be equal to $\phi$. In this case, the satellite's orientation would be given simply by the mean anomaly $\theta(t) = nt$. The presence of longitudinal torques, however, causes small additional variations in the satellite's orientation so that $\theta(t) = nt + \gamma(t)$, where $\gamma$ is the forced physical libration. Assuming for now that n is constant (although a discussion on perturbations from other satellites is provided below), we have $\ddot{\theta} = \ddot{\gamma}$.

The satellite's true anomaly (Fig. 5a), expanded as a Fourier series and limited to first order in eccentricity (*Murray and Dermott,* 1999), is given by

$$f = nt + 2e \sin nt + 0\left(e^2\right) \qquad (32)$$

It is clear from Fig. 5a that $f–\theta = \psi$, so that $\psi = 2e \sin nt – \gamma$. Using the small angle approximation for $\psi$, equation (31) can be rewritten

$$\ddot{\theta} = \frac{3(B-A)}{C} \frac{Gm}{r^3} \left(2e \sin nt - \gamma\right) \qquad (33)$$

With the approximation that $Gm \approx r^3 n^2$, and given that $\ddot{\theta} = \ddot{\gamma}$, this yields

$$\ddot{\gamma} = 2e\omega_0^2 \sin nt - \gamma\omega_0^2 \qquad (34)$$

where $\omega_0$ is the natural frequency, defined as

$$\omega_0 = n\sqrt{\frac{3(B-A)}{C}} \qquad (35)$$

Finally, substituting $\gamma = \gamma_0 \sin nt$ into equation (34), the solution becomes

$$\gamma = \frac{2e}{1 - \left(n/\omega_0\right)^2} \sin nt \qquad (36)$$

The amplitude of the forced physical libration thus depends on the natural frequency $\omega_0$, which is a function of the moments of inertia via equation (35), and hence the satellite's interior structure. Note that the phase of the physical libration is a function of n and $\omega_0$: If $n < \omega_0$, then the libration would be in phase with the torque, while if $n > \omega_0$, the libration and the torque would be 180° out of phase (*Murray and Dermott,* 1999, p. 216), which is the case for Enceladus and the case illustrated in Fig. 5b.

So far, we have considered only the two-body problem, where the satellite's motion is not perturbed by other satellites. The more general expression of the physical libration is (*Rambaux et al.,* 2010)

$$\gamma = A_d \sin\left(\omega_d t + \alpha_d\right) e^{-\lambda t}$$
$$+ \sum_i \frac{H_i}{1 - \left(\omega_i/\omega_0\right)^2} \sin\left(\omega_i t + \alpha_i\right) \qquad (37)$$

The first term in equation (37) represents the free libration of the satellite, usually induced by episodic events such as impacts. The free libration oscillates at $\omega_d = \sqrt{\omega_0^2 - \lambda^2}$, also called the free libration frequency, very close to the satellite's natural frequency $\omega_0$ [$\lambda$ is a damping constant (*Rambaux et al.,* 2010)]. The amplitude $A_d$ and the phase $\alpha_d$ are integration constants that are functions of the initial conditions related to the perturbing event. Since dissipation in the satellite will damp the free librations on a timescale of tens of years (*Rambaux et al.,* 2010; *Noyelles et al.,* 2011), we can assume that the observed librations of Enceladus are forced.

The second term in equation (37) represents the forced libration, including gravitational perturbations from other satellites. Such perturbations introduce additional librations, where $H_i$, $\omega_i$, and $\alpha_i$ are the magnitude, frequency, and phase of the $i^{th}$ perturbation, respectively. Equation (36) is a special case of equation (37), corresponding to the orbital frequency, n, and an amplitude of $H_i = 2e$. Using the JPL Horizons Ephemeris (*http://ssd.jpl.nasa.gov/horizons.cgi*), *Rambaux et al.* (2010) identified three major libration frequencies for Enceladus, with periods of 1.37 days, 3.89 years, and 11.05 years, and respective amplitudes of –0.028°, 0.189°, and 0.259° (based on a solid-body interior model). The first signal, at the orbital period of Enceladus, is due to the mean anomaly perturbation. The comparison to the semi-analytical model of Enceladus' orbit (*Vienne and Duriez,* 1995) suggests that the remaining two signals are due to the Enceladus-Dione resonance: The first is related to Dione's precession of pericenter, and the second is related to the orbital libration argument of the Dione-Enceladus resonance.

Equation (37) indicates that the forced libration amplitudes, at all frequencies, depend on the natural frequency $\omega_0$, and thus on the satellite's internal structure. However, because the amplitude depends on $1–(\omega_i/\omega_0)^2$, the effect is only significant for the libration at the orbital frequency, for which $(\omega_i/\omega_0)^2$ is non-negligible (Table 4). For this reason, in attempting to constrain the interior structure, we focus only on the libration at the satellite's orbital period.

### 3.2. Measuring Physical Librations

With the exceptions of Mercury (*Margot et al.,* 2007) and the Moon (*Dickey et al.,* 1994), all measurements of physical libration amplitudes have been carried out by photogrammetry using spacecraft imagery (*Tiscareno et al.,* 2009; *Willner et al.,* 2010; *Nadezhdina and Zubarev,* 2014; *Tajeddine et al.,* 2014; *Thomas et al.,* 2016). This technique uses images to

TABLE 4. Dominant signals involved in the forced librations of Enceladus (*Rambaux et al., 2010*).

| Period (days) | Amplitude (deg) | $(\omega_i/\omega_0)^2$ |
|---|---|---|
| 1.37 | −0.028 | 16.3 |
| 1418.93 | 0.188 | $1.5 \times 10^{-5}$ |
| 4035.64 | 0.259 | $1.9 \times 10^{-6}$ |

Because $(\omega_i/\omega_0)^2$ is negligibly small for the longer-period librations, only the libration at the orbital period is significantly determined by the internal structure, via equation (35).

build three-dimensional coordinates of recognizable surface features, called control points, by observing them from various angles. With sufficient coverage, a global control point network can be built and used for mapping and for generating digital terrain models (DTMs). Like any observation-based technique, control points are subject to reconstruction errors. While some are random, others are systematic, such as errors in spacecraft position, camera pointing, and the body's rotation model (including the effect of any physical libration).

During its time in the Saturn system, the Cassini spacecraft collected tens of thousands of images of Enceladus. Observations were made from various phase angles and distances, in order to study the plumes, surface geology, and orbital and rotational dynamics. The amplitude of the physical libration of Enceladus is on the order of hundreds of meters of surface displacement at the equator. The spacecraft must be close enough to obtain images of sufficiently high resolution to permit libration detection. However, the spacecraft must not be too close, because when only a small part of the surface is in view, all the predicted positions of control points projected onto that image have nearly the same systematic errors, preventing the fitting software from distinguishing between libration-related offsets and camera-pointing errors. Provided that a sufficient latitudinal range is in view, however, the ambiguity is removed because, unlike camera pointing errors, the libration-related offsets vary with latitude.

To measure the physical librations of Enceladus, *Thomas et al.* (2016) used a network of 488 control points (mostly craters) across the surface, tracking them through a series of 340 Cassini Imaging Science Subsystem (ISS) images, totaling 5873 measurements. Starting from the approximately known positions of each control point in the satellite's reference frame, the control points were first converted to J2000, a fixed frame based on the initial conditions of Earth's rotational state on January 1, 2000, at 12:00 Terrestrial Time. This requires knowledge of the satellite's rotational parameters (i.e., orientation of the spin axis, rotation rate, librations, etc.), accounting for the three major libration frequencies (Table 4). As discussed above, the amplitudes of the long-period librations are well known since their dependence on Enceladus' interior is negligible. The amplitude of the signal at the orbital period of Enceladus (including the physical libration), however, is a parameter that needs to be fitted. Next, the coordinates are converted to the reference frame of the Cassini ISS Narrow Angle Camera (NAC), requiring instantaneous information of the spacecraft's position and the camera's pointing angle. This information is available at NASA's Navigation and Ancillary Information Facility (NAIF) SPICE website (*http://naif.jpl.nasa.gov/naif*). The twist angle (orientation about the axis along the line of sight) of the Cassini NAC is well determined, and the position of the spacecraft is known to within 1–10 km. The camera's right ascension and declination, however, are not well determined and must be fitted.

Next, the three-dimensional coordinates of the control points were adjusted in order to minimize the $\chi^2$ residuals between the observed and predicted positions of the control points projected onto the camera image plane. To avoid degeneracies associated with going from three dimensions to two, each control point must have been observed from at least two sufficiently different viewing geometries. The more a control point is observed in different images, the lower the uncertainties in its position. Similarly, increasing the number of control points in an image reduces the uncertainties on camera-pointing angle. Finally, the reconstructed control point network still depends on the assumed rotational model for the satellite. When the model does not describe the satellite's rotation accurately, additional errors will result in the reconstructed positions of control points. Therefore, the libration amplitude at the orbital period must be varied in order to minimize the reconstruction errors.

Following this procedure, *Thomas et al.* (2016) obtained a best-fit physical libration amplitude of −0.120° (the minus sign indicates that the libration is out of phase by 180°) with a 2σ uncertainty of 0.014°. This translates to 528 ± 60 m in surface displacement at the equator. The smallness of the uncertainty is a function of the fact that the control points are based on ellipses fitted to craters, permitting subpixel accuracy in their positions and, more importantly, the large number of data points (since the uncertainty goes as $N^{-1/2}$).

### 3.3. Interior Modeling and Interpretation

Having measured the libration amplitude, we can now compute the satellite's natural frequency via equation (34) and hence determine its dynamical triaxiality, (B–A)/C, via equation (35). The value corresponding to the observed libration amplitude of 0.120° is (B–A)/C ≈ 0.0607. Although fixing this quantity does not yield a unique interior model, various simple trial models can be tested to determine the approximate internal structure.

Assuming a multi-layered body consisting of nested triaxial ellipsoids, the principal moments of inertia, defined in equation (3), become

$$A = \frac{4\pi}{15} \sum_i \Delta\rho_i \left( b_i^2 + c_i^2 \right) a_i b_i c_i$$

$$B = \frac{4\pi}{15} \sum_i \Delta\rho_i \left( a_i^2 + c_i^2 \right) a_i b_i c_i \qquad (38)$$

$$C = \frac{4\pi}{15} \sum_i \Delta\rho_i \left( a_i^2 + b_i^2 \right) a_i b_i c_i$$

where $a_i$, $b_i$, and $c_i$ are the semiaxes of the $i^{th}$ ellipsoid, and $\Delta\rho_i$ is the density contrast between layer i and the layer above it. In the simplest case of a homogeneous interior, the dynamical triaxiality is simply

$$\frac{B - A}{C} = \frac{a^2 - b^2}{a^2 + b^2} \qquad (39)$$

Based on their shape model, in which a = 256.2 km, and b = 251.4 km, *Thomas et al.* (2016) found that the libration amplitude expected for a homogenous interior was ~0.032° — more than 10σ smaller than the observed value. In the case of a two-layer body, the triaxiality is given by

$$\frac{B - A}{C} = \frac{V\rho_s\left(a_s^2 - b_s^2\right) + V_c\left(\rho_c - \rho_s\right)\left(a_c^2 - b_c^2\right)}{V\rho_s\left(a_s^2 + b_s^2\right) + V_c\left(\rho_c - \rho_s\right)\left(a_c^2 + b_c^2\right)} \qquad (40)$$

where the subscripts c and s indicate the rocky core and the icy shell, respectively, V is the volume, and ρ is the density. Unlike the case of a homogeneous interior, models with two or more layers require additional assumptions about the shape and densities of each layer. The known bulk density (1609 kg m$^{-3}$ for Enceladus) and the inferred moment of inertia factor constrain, via equations (1) and (2), the layer thicknesses such that the core radius can be computed once the layer densities are specified. Computing the shapes of internal layers is less straightforward but can be done in a number of ways. *Thomas et al.* (2016) and *van Hoolst et al.* (2016), for instance, integrate the Clairaut equation (*Clairaut,* 1743; *Danby,* 1988) to first order in terms of the polar and equatorial flattening to obtain expressions that depend only on the densities and mean radii of the layers, which can then be related to the semiaxes of the triaxial ellipsoidal shape (for details, see *Tajeddine et al.,* 2014). Similarly, *Tricarico* (2014) describes methods for computing higher-order nested ellipsoidal figures recursively or numerically in terms of polar and equatorial eccentricities, again, starting from the specified densities and mean radii of each layer.

Making the assumption that the core shape conforms to the hydrostatic expectation (i.e., its surface is equipotential), and considering a range of ice shell densities between 700 kg m$^{-3}$ and 930 kg m$^{-3}$, *Thomas et al.* (2016) determined that the libration amplitude for the two-layer model would be between 0.032° and 0.034°, still much smaller than the observed value. Thomas et al. further showed that a regional subsurface sea centered on the south pole has little effect on the libration amplitude because of its symmetry about the axis of rotation. Similar results were obtained by *van Hoolst et al.* (2016), confirming the incompatibility of the libration observations with interior models involving a core that is physically coupled to the icy mantle.

As another check, one can use the above dynamical triaxiality in combination with the observed sectorial gravity harmonic, $C_{22}$ (Table 1), and equation (22) to compute the polar moment of inertia. The result is C ≈ 0.104M R$^2$. This unrealistically small polar moment of inertia is not compatible with the internal density structure inferred from the gravity observations [roughly 0.22M R$^2$ (*Iess et al.,* 2014; *McKinnon,* 2015)] and is another indication that Enceladus is not behaving like an entirely solid body.

The large observed libration amplitude evidently requires a more radically different interior model. *Thomas et al.* (2016) thus argued for a model with a global subsurface ocean that completely decouples the rocky core from the icy shell. In this case, the icy shell and the rocky core experience and respond to gravitational torques nearly independently. In the limit of a spherical core, for example, only the shell itself experiences external gravitational torques and, because the polar moment of inertia for the shell alone, $C_s$, is smaller than that of the body as a whole, C, the libration amplitude should be larger.

*Thomas et al.* (2016) and *van Hoolst et al.* (2016) applied a more generalized analysis, which includes the effects of torques between the shell and the core, as well as the effects of the ocean pressure on both the core and the shell. For a body with a subsurface ocean decoupling the shell from the core, the libration amplitude of the shell is given by (e.g., *van Hoolst et al.,* 2009; *Rambaux et al.,* 2011; *Richard et al.,* 2014)

$$\gamma_s = \frac{2e\left[K_s\left(K_c + 2K_{int} - n^2C_c\right) + 2K_{int}K_c\right]}{C_cC_s\left(n^2 - \omega_1^2\right)\left(n^2 - \omega_2^2\right)} \qquad (41)$$

where $K_s$, $K_c$, and $K_{int}$ are the planet-shell, planet-core, and core-shell torques, respectively. The first two torques are functions of the moments of inertia of the shell and the core, as well as the ocean pressure on each layer; $K_{int}$ depends on the densities and the dimensions of each layer; and $\omega_1$ and $\omega_2$ are the system's natural frequencies (for details, see *Richard et al.,* 2014).

This expression shows that the libration amplitude once again depends on the densities assumed for the internal layers as well as their shapes. Assuming hydrostatic figures for each layer and assuming the ice shell and ocean densities to be 850 kg m$^{-3}$ and 1000 kg m$^{-3}$, respectively, *Thomas et al.* (2016) found the best agreement with the observed librations for interior models with mean ice shell thicknesses in the range 21–26 km and mean ocean thicknesses in the range 26–31 km. The densities of the ice shell and the core were adjusted (within the constraints noted above) to 850 kg m$^{-3}$ and 2300 kg m$^{-3}$, respectively, in order to be consistent with the moment of inertia inferred from the gravity observations (*Iess et al.,* 2014). Using similar methods, but considering different ranges of core, ice shell, and ocean densities (2158–2829 kg m$^{-3}$, 900–1000 kg m$^{-3}$, and 950–1100 kg m$^{-3}$, respectively), and allowing for non-hydrostatic figures for the core and the ocean/ice interface, *van Hoolst et al.* (2016) obtained mean ice shell and ocean thicknesses in the ranges 14–21 km and 24–67 km, respectively.

Although results vary slightly with the assumptions that go into such models, it is clear that the observed physical libration amplitude places powerful constraints on the internal structure. Most importantly, these libration studies demonstrate that the ice shell must be fully decoupled from the deeper interior, requiring the subsurface ocean to be global. Additionally, the libration studies provide a means of estimating the ice shell's thickness in a manner that is independent from the gravity-based analysis discussed in section 2, increasing confidence in both approaches.

## 4.  ICE SHELL STRUCTURE AND DYNAMICS

### 4.1.  Structure

The structure of the ice shell is of particular interest because it bears on the thermal state of Enceladus, the means for supporting its topography, the mechanics of the major fissures in the south polar region, and the nature of the ongoing eruptions. Determining the precise thickness of the ice shell, however, is not necessarily straightforward. For example, analysis of Enceladus' gravity field (section 2) has yielded mean shell thickness estimates ranging from 20–40 km (*Iess et al.,* 2014) at the low end, to 40–60 km (*McKinnon*, 2015) at the high end (although the latter estimate is based only on the degree-2 gravity). The large amplitude of the diurnal forced physical librations (section 3) (*Thomas et al.,* 2016; *van Hoolst et al.,* 2016), on the other hand, suggests a mean shell thickness of 15–25 km. The apparent discrepancy is not as problematic as it may seem, however, as it can be resolved in a number of ways involving details of the elastic/isostatic compensation model (*Čadek et al.,* 2016; *Beuthe et al.,* 2016; *Hemingway and Mittal,* 2017), as discussed in section 2.3.3.

What is common among the various models is that they take the long-wavelength topography to be related to lateral variations in the thickness of the icy shell, which is, to some degree, supported isostatically (i.e., it is "floating" on a subsurface ocean). Hence, the large topographic basin at the south pole implies a regional thinning of the ice shell, as predicted by *Collins and Goodman* (2007) based on the observed shape (*Thomas et al.,* 2007) and the localized geologic activity. The gravity observations (*Iess et al.,* 2014) confirmed this prediction by showing that the small magnitude of the corresponding south polar gravity anomaly implied substantial compensation (i.e., thinning at the base of the ice shell). Given the ~2-km topographic depression at the south pole (measured with respect to an equilibrium figure) (*Nimmo et al.,* 2011), and making reasonable assumptions about the ice shell and ocean densities, the total crustal thinning (relative to the mean shell thickness) at the south pole must be roughly 16–18 km, assuming complete Airy-type isostatic compensation (see equation (28) in section 2.3.3) (*Čadek et al.,* 2016; *Hemingway and Mittal,* 2017). Since the shell thickness is evidently greater than zero at the south pole, this may be regarded as an approximate lower bound on the mean shell thickness. However, the precise amplitude of lateral shell thickness variations also depends on the assumed compensation model (i.e., pressure vs. force balance, inclusion of partial elastic support, lateral variations in crustal density, etc.) (*Čadek et al.,* 2016; *Hemingway and Matsuyama,* 2017; *Hemingway and Mittal,* 2017; *Tajeddine et al.,* 2017).

The various models also agree that the thickest part of the shell is around the equator, and especially near the sub- and anti-saturnian points, where the thickness may be 30–40 km, or even more, depending on the preferred compensation model (*Čadek et al.,* 2016; *Hemingway and Mittal,* 2017). The overall pattern (Fig. 6) may be the result, at least in part, of tidal heating. Tidal dissipation is strongest at the poles and weaker in the equatorial regions (*Ojakangas and Stevenson,* 1989). The equilibrium shell thickness based on tidal dissipation and insolation results in a pattern with power at degrees 2 and 4 (*Ojakangas and Stevenson,* 1989; *Hemingway and Mittal,* 2017). Higher-order structure in the shell thickness variations may be a result of heterogeneities in the shell and/or mode coupling associated with non-Newtonian flow of the ice as it relaxes (*Nimmo,* 2004).

### 4.2.  Thermal and Mechanical Stability

The structure of the ice shell raises questions about the stability of the current configuration. Lateral shell thickness variations induce stresses that will tend to relax away those thickness variations over time, with the ice flowing from the thicker regions (i.e., the equator) to the thinner regions (i.e., the poles). The observed structure is thus stable only if the relaxation rate is counterbalanced by spatial variations in ice melting (associated with tidal dissipation) and ocean crystallization rates (e.g., *Collins and Goodman,* 2007; *Kamata and Nimmo,* 2017). The rate at which the deflected ice/ocean interface relaxes toward an equipotential surface is controlled by the viscosity structure of the ice shell. Following the approach of *Lefevre et al.* (2014), developed for Titan, *Čadek et al.* (2016) determined that the relaxation velocity remains smaller than a few centimeters per year only if the ice shell is conductive with a bottom viscosity of at least $10^{14}$–$10^{15}$ Pa s. Counterbalancing such a relaxation rate requires heat flux variations between the equatorial and polar regions of at least 100–200 mWm$^{-2}$, which is comparable with the estimated heat flux in the SPT.

It is also possible that the current configuration is transient, with the observed surface topography being the partially relaxed remnants of a previous state with larger thickness variations (*Čadek et al.,* 2016). *Čadek et al.* (2017) have argued, using a viscoelastic relaxation model, that the observed surface topography may be presently relaxing toward a new equilibrium if Enceladus experiences changes in heat production and ice melting/ocean crystallization on timescales comparable to the relaxation timescale (which may range between 1 and 100 m.y. for lithospheric viscosities between $10^{22}$ and $10^{24}$ Pa s). Indeed, the intense
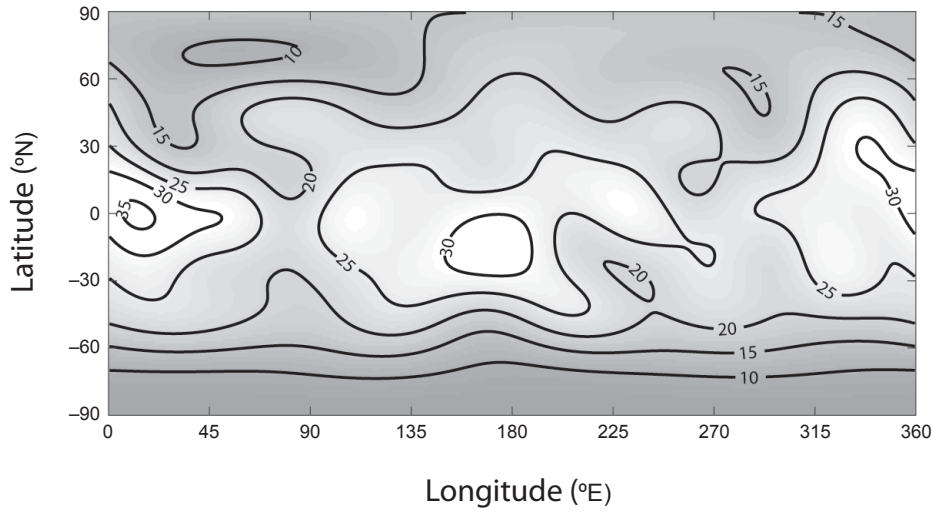
**Fig. 6.** Lateral variations in ice shell thickness assuming complete Airy compensation of all known topography [up to spherical harmonic degree 8 (*Nimmo et al., 2011*)]. Contours indicate shell thickness in kilometers. In this example, the ice shell thickness ranges from ~6 km at the south pole to ~36 km at the sub- and anti-saturnian points along the equator, with a mean thickness of 22 km. While the mean shell thickness is somewhat model-dependent, the amplitude of lateral variation does not vary significantly among the models (e.g., *Čadek et al.,* 2016; *Hemingway and Mittal,* 2017). The addition of partial elastic support, however, would alter the amplitude of shell thickness variations, especially at the shortest wavelengths.

surface activity in the south polar region is an indication of a dynamical world where the ice shell structure may be evolving on even shorter timescales.

### 4.3. Implications

The shell thickness implies a small Rayleigh number, making convection unlikely and suggesting a thermally conductive ice shell. Heat flux, F, can be related to the temperature structure and thickness of a conductive ice shell according to

$$F = \frac{c}{d} \ln\left(\frac{T_s}{T_b}\right) \qquad (42)$$

where d is the shell thickness, $T_s$ and $T_b$ are the surface and basal temperatures, respectively, and where c is an empirically derived constant, taken to be 567 W/m (e.g., *Klinger,* 1980; *Nimmo,* 2004). For an ice shell thickness of about 30–40 km in the equatorial region, the diffusive heat flux typically ranges between 15 and 20 mWm$^{-2}$. As the diffusive heat loss is inversely proportional to the ice shell thickness, cooling is even faster away from the equator, where the shell is thinner. For an average ice shell thickness between 20 and 25 km, the total diffusive heat loss outside the SPT is about 20 GW. In addition to the passive heat loss, one must also consider the heat loss associated with the intense activity at the south pole, which is estimated to be up to 15 GW (*Howett et al.,* 2011). For ice shell thicknesses ranging be-

tween 3 and 5 km in the SPT, about 5 to 10 GW is lost just by thermal diffusion through the ice shell, with the rest of the power being associated with the eruption activity itself. In total, then, some ~35 GW must be generated to maintain the present-day state of Enceladus.

Such a large power is consistent with the latest estimates of the dissipation function in Saturn (*Lainey et al.,* 2012; *Lainey,* 2016), which indicates that a strong dissipation (20 GW or even more) may be sustained during relatively long periods of time before the orbital eccentricity would be damped. However, the mechanism for generating such power within Enceladus is less clear (see the chapter in this volume by Nimmo et al.). Such heat production in the ice shell would require a very low bottom viscosity [<5 × 10$^{13}$ Pa s (*Roberts and Nimmo,* 2008)], which would result in rapid relaxation of the basal topography, incompatible with the observed thickness variations. On the other hand, for a bottom viscosity ranging between 10$^{14}$ and 10$^{15}$ Pa s, heat flow due to tidal dissipation in the conductive ice shell would barely exceed a few milliwatts per square meter (*Roberts and Nimmo,* 2008; *Čadek et al.,* 2016), too weak to counterbalance the diffusive heat loss and to prevent the ocean from freezing (the timescale to crystallize 10 km of ice in the thickest part of the ice shell is on the order of 10 m.y.). The present-day state may result from enhanced tidal dissipation due to higher eccentricities in the recent past, as suggested by *Běhounková et al.* (2012). This would imply that the ocean is presently crystallizing with a maximum crystallization rate in the equatorial region where tidal heating is at a minimum.

An alternative solution would be strong dissipation in the deeper interior that counterbalances the diffusive heat loss through the ice shell. Two candidate processes would be dissipation of resonant tidal waves in the ocean (*Tyler,* 2011; *Matsuyama,* 2014; *Hay and Matsuyama,* 2017) or tidal friction in the unconsolidated core (*Roberts,* 2015). The former process requires a thin ocean, contrary to the ocean thickness inferred by recent studies (*Čadek et al.,* 2016; *van Hoolst et al.,* 2016; *Beuthe et al.,* 2016; *Hemingway and Mittal,* 2017). For the latter process, an unconsolidated rocky core filled with water ice, the power produced is too low (*Roberts,* 2015). Dissipation in a water-filled porous core might be more efficient, but more work is needed to demonstrate whether this would be sufficient to counterbalance the diffusive heat loss. Interestingly, strong dissipation in the core may also provide the energy source to power the hydrothermal activity, as suggested by the detection of nanosilica emitted from Enceladus (*Hsu et al.,* 2015), and to sustain long-term circulation of hot water in the core, as modeled by *Travis and Schubert* (2015).

An interesting consequence of the reduced ice shell thickness in the SPT is a strong increase of tidal deformation and associated tidal friction. Compared to models with constant thickness of 25 km, the reduction in the SPT to less than 5 km in thickness results in an amplification of the tidal stresses by a factor of 4 (*Soucek et al.,* 2017). This is a consequence of the small size of Enceladus, which makes the amplitude of tidal deformation much more sensitive to the ice shell thickness than in larger moons like Europa and Titan, where tidal deformation depends only slightly on the ice shell thickness (*Tobie et al.,* 2005). *Soucek et al.* (2016) have also demonstrated that the presence of faults further enhances the tidal deflections by at least a factor of 2. The resulting stress patterns are much more complex than those predicted from standard tidal deformation models based on a thin-shell approximation and neglecting the presence of faults (e.g., *Hurford et al.,* 2007; *Nimmo et al.,* 2007). Enhanced tidal stresses in the SPT, together with lithospheric stresses resulting from ice shell melting and subsequent relaxation, may help explain the tectonic patterns observed in the SPT (e.g., *Patthoff and Kattenhorn,* 2011; *Yin et al.,* 2016). However, future modeling efforts are required to better understand the complex interplay between the ice shell evolution and the tectonic patterns.

## 5. SUMMARY AND OPEN QUESTIONS

The Cassini mission has helped to answer many questions about the interior of Enceladus. In particular, as we discussed in this chapter, Cassini-derived measurements of the low-order gravity field and rotational dynamics have led to a good, albeit basic, understanding of the internal structure (Fig. 1). We now know, for instance, that Enceladus has a large, low-density core that is in contact with a global subsurface liquid water ocean containing some $10^7$ km$^3$ of water (section 2.3.4) — comparable to the volume of Earth's Arctic Ocean. The icy shell that covers the ocean may be vanishingly thin at the south pole, but is at least a few tens of kilometers thick in the equatorial regions (Fig. 6).

Nevertheless, the thickness, structure, and dynamics of the ice shell are not yet sufficiently well constrained to give us a clear understanding of the thermal history and evolution of the interior. Is the current configuration stable, or are we seeing Enceladus in the midst of a transition? If the present configuration is stable, how is the long-wavelength topography maintained in spite of the relatively high temperatures at the base of the ice shell? How and where is the internal heat generated, and can we match the predicted input power with the estimated heat loss? In the near term, additional modeling efforts may help to better address these questions. In the longer term, when spacecraft next visit Enceladus, and especially with dedicated missions that can orbit or even land on Enceladus, new observations — which may include higher-order gravity measurements, improved heat flow measurements, ice penetrating radar, and even seismology — are sure to be the most powerful drivers in advancing our understanding of the interior of Enceladus.

## REFERENCES

Anderson J. D., Schubert G., Jacobson R. A., Lau E. L., Moore W. B., and Sjogren W. L. (1998) Europa's differentiated internal structure: Inferences from four Galileo encounters. *Science, 281(5385),* 2019–2022, DOI: 10.1126/science.281.5385.2019.

Baland R. M., Yseboodt M., and Van Hoolst T. (2016) The obliquity of Enceladus. *Icarus, 268,* 12–31, DOI: 10.1016/j.icarus.2015.11.039.

Baum W. A., Kreidl T., Westphal J. A., Danielson G. E., Seidelmann P. K., Pascu D., and Currie D. G. (1981) Saturn's E ring: I. CCD observations of March 1980. *Icarus, 47(1),* 84–96, DOI: 10.1016/0019-1035(81)90093-2.

Běhounková M., Tobie G., Choblet G., and Čadek O. (2012) Tidally-induced melting events as the origin of south-pole activity on Enceladus. *Icarus, 219(2),* 655–664, DOI: 10.1016/j.icarus.2012.03.024.

Besserer J., Nimmo F., Roberts J. H., and Pappalardo R. T. (2013) Convection-driven compaction as a possible origin of Enceladus's long wavelength topography. *J. Geophys. Res.–Planets, 118(5),* 908–915, DOI: 10.1002/jgre.20079.

Beuthe M. (2008) Thin elastic shells with variable thickness for lithospheric flexure of one-plate planets. *Geophys. J. Intl., 172(2),* 817–841, DOI: 10.1111/j.1365-246X.2007.03671.x.

Beuthe M., Rivoldini A., and Trinh A. (2016) Enceladus' and Dione's floating ice shells supported by minimum stress isostasy. *Geophys. Res. Lett., 43,* DOI: 10.1002/2016GL070650.

Brown R. H. et al. (2006) Composition and physical properties of Enceladus' surface. *Science, 311(5766),* 1425–1428, DOI: 10.1126/science.1121031.

Buratti B. and Veverka J. (1984) Voyager photometry of Rhea, Dione, Tethys, Enceladus and Mimas. *Icarus, 58,* 254–264, DOI: 10.1016/0019-1035(84)90042-3.

Burša M. and Peč K. (1993) *Gravity Field and Dynamics of the Earth.* Springer, New York. 333 pp.

Čadek O. et al. (2016) Enceladus's internal ocean and ice shell constrained from Cassini gravity, shape and libration data. *Geophys. Res. Lett., 43,* DOI: 10.1002/2016GL068634.

Čadek O., Běhounková M., Tobie G., and Choblet G. (2017) Viscoelastic relaxation of Enceladus's ice shell. *Icarus, 291,* 31–35, DOI: 10.1016/j.icarus.2017.03.011.

Chen E. M. A. and F. Nimmo (2011) Obliquity tides do not significantly heat Enceladus. *Icarus, 214(2),* 779–781, DOI: 10.1016/j.icarus.2011.06.007.

Clairaut A. C. (1743) *Theorie de la figure de la Terre, Tirée des principes de l'Hydrostatique,* Paris.

Clark R. N., Brown R. H., Nelson M. L., and Hayashi J. N. (1983) Surface composition of Enceladus. *Bull. Am. Astron. Soc., 15,* 853.

Collins G. C. and Goodman J. C. (2007) Enceladus' south polar sea. *Icarus, 189(1),* 72–82, DOI: 10.1016/j.icarus.2007.01.010.

Dahlen F. A. (1982) Isostatic geoid anomalies on a sphere. *J. Geophys. Res., 87(B5),* 3943–3947, DOI: 10.1029/JB087iB05p03943.

Danby J. M. A. (1988) *Fundamentals of Celestial Mechanics.* Willman-Bell, Richmond. 348 pp.

Darwin G. H. (1899) The theory of the figure of the Earth carried to the second order of small quantities. *Mon. Not. R. Astron. Soc., 60,* 82–124.

Dickey J. O. et al. (1994) Lunar Laser Ranging: A continuing legacy of the Apollo program. *Science, 265(5171),* 482–490.

Dougherty M. K., Khurana K. K., Neubauer F. M., Russell C. T., Saur J., Leisner J. S., and Burton M. E. (2006) Identification of a dynamic atmosphere at Enceladus with the Cassini magnetometer. *Science, 311(5766),* 1406–1409, DOI: 10.1126/science.1120985.

Gladman B., Quinn D. D., Nicholson P., and Rand R. (1996) Synchronous locking of tidally evolving satellites. *Icarus, 122,* 166–192, DOI: 10.1006/icar.1996.0117.

Haff P. K., Eviatar A., and Siscoe G. L. (1983) Ring and plasma: The enigmae of Enceladus. *Icarus, 56(3),* 426–438, DOI: 10.1016/0019-1035(83)90164-1.

Hansen C. J., Esposito L., Stewart A. I. F., Colwell J., Hendrix A., Pryor W., Shemansky D., and West R. (2006) Enceladus' water vapor plume. *Science, 311,* 1422–1425, DOI: 10.1126/science.1121254.

Hay H. C. F. C. and Matsuyama I. (2017) Numerically modelling tidal dissipation with bottom drag in the oceans of Titan and Enceladus. *Icarus, 281,* 342–356, DOI: 10.1016/j.icarus.2016.09.022.

Hemingway D. J. and Matsuyama I. (2017) Isostatic equilibrium in spherical coordinates and implications for crustal thickness on the Moon, Mars, Enceladus, and elsewhere. *Geophys. Res. Lett., 44,* 7695–7705, DOI: 10.1002/2017GL073334.

Hemingway D. J. and Mittal T. (2017) What explains the structure of Enceladus's ice shell and can it be in equilibrium? Abstract P43B-2877 presented at 2017 Fall Meeting, AGU, New Orleans, Louisiana, 11–15 December.

Hemingway D., Nimmo F., Zebker H., and Iess L. (2013a) A rigid and weathered ice shell on Titan. *Nature, 500(7464),* 550–552, DOI: 10.1038/nature12400.

Hemingway D., Nimmo F., and Iess L. (2013b) Enceladus' internal structure inferred from analysis of Cassini-derived gravity and topography. Abstract P53E-03 presented at 2013 Fall Meeting, AGU, San Francisco, California, 9–13 December.

Hemingway D. J., Zannoni M., Tortora P., Nimmo F., and Asmar S. W. (2016) Dione's internal structure inferred from Cassini gravity and topography. In *Lunar and Planetary Science XLVII,* Abstract #1314. Lunar and Planetary Institute, Houston.

Howett C. J. A., Spencer J. R., Pearl J., and Segura M. (2011) High heat flow from Enceladus' south polar region measured using 10–600 cm$^{-1}$ Cassini/CIRS data. *J. Geophys. Res.–Planets, 116(3),* 1–15, DOI: 10.1029/2010JE003718.

Hsu H.-W. et al. (2015) Ongoing hydrothermal activities within Enceladus. *Nature, 519(7542),* 207–210, DOI: 10.1038/nature14262.

Hubbard W. B. (1984) *Planetary Interiors.* Van Nostrand Reinhold, New York. 334 pp.

Hurford T. A., Helfenstein P., Hoppa G. V., Greenberg R., and Bills B. G. (2007) Eruptions arising from tidally controlled periodic openings of rifts on Enceladus. *Nature, 447(7142),* 292–294, DOI: 10.1038/nature05821.

Iess L., Rappaport N. J., Jacobson R. A., Racioppa P., Stevenson D. J., Tortora P., Armstrong J. W., and Asmar S. W. (2010) Gravity field, shape, and moment of inertia of Titan. *Science, 327(5971),* 1367–1369, DOI: 10.1126/science.1182583.

Iess L., Jacobson, Ducci M., Stevenson D. J., Lunine J. I., Armstrong J. W., Asmar S. W., Racioppa P., Rappaport N. J., and Tortora R. A. P. (2012) The tides of Titan. *Science, 337,* 457–459, DOI: 10.1126/science.1219631.

Iess L. et al. (2014) The gravity field and interior structure of Enceladus. *Science, 344(6179),* 78–80, DOI: 10.1126/science.1250551.

Jacobson R. A. (2004) The orbits of the major saturnian satellites and the gravity field of Saturn from spacecraft and Earth-based observations. *Astron. J., 128,* 492–501, DOI: 10.1086/421738.

Jeffreys H. (1976) *The Earth: Its Origin, History, and Physical Constitution,* 6th edition. Cambridge Univ., New York. 612 pp.

Kamata S. and Nimmo F. (2017) Interior thermal state of Enceladus inferred from the viscoelastic state of the ice shell. *Icarus, 284,* 387–393, DOI: 10.1029/2011JE003835.

Klinger J. (1980) Influence of a phase transition of ice on the heat and mass balance of comets. *Science, 209(4453),* 271–272.

Kozai Y. (1976) Masses of satellites and oblateness parameters of Saturn. *Publ. Astron. Soc. Japan, 28,* 675–691.

Lainey V. (2016) Quantification of tidal parameters from solar system data. *Cel. Mech. Dyn. Astron., 126(1),* 1–12, DOI: 10.1007/s10569-016-9695-y.

Lainey V. et al. (2012) Strong tidal dissipation in Saturn and constraints on Enceladus' thermal state from astrometry. *Astrophys. J., 752(14),* DOI: 10.1088/0004-637X/752/1/14.

Lefevre A., Tobie G., Choblet G., and Cadek O. (2014) Structure and dynamics of Titan's outer icy shell constrained from Cassini data. *Icarus, 237,* 16–28, DOI: 10.1016/j.icarus.2014.04.006.

Margot J. L., Peale S. J., Jurgens R. F., Slade M. A, and Holin I. V. (2007) Large longitude libration of Mercury reveals a molten core. *Science, 316(5825),* 710–714, DOI: 10.1126/science.1140514.

Martinec Z. (1994) The density contrast at the Mohorovičič discontinuity. *Geophys. J. Intl., 117(2),* 539–544, DOI: 10.1111/j.1365-246X.1994.tb03950.x.

Matsuyama I. (2014) Tidal dissipation in the oceans of icy satellites. *Icarus, 242,* 11–18, DOI: 10.1016/j.icarus.2014.07.005.

McKinnon W. B. (2013) The shape of Enceladus as explained by an irregular core: Implications for gravity, libration, and survival of its subsurface ocean. *J. Geophys. Res.–Planets, 118,* 1775–1788, DOI: 10.1002/jgre.20122.

McKinnon W. B. (2015) Effect of Enceladus's rapid synchronous spin on interpretation of Cassini gravity. *Geophys. Res. Lett., 42,* DOI: 10.1002/2015GL063384.

Meyer J. and Wisdom J. (2007) Tidal heating in Enceladus. *Icarus, 188(2),* 535–539, DOI: 10.1016/j.icarus.2007.03.001.

Murray C. D. and Dermott S. F. (1999) *Solar System Dynamics.* Cambridge Univ., Cambridge.

Nadezhdina I. E. and Zubarev A. E. (2014) Formation of a reference coordinate network as a basis for studying the physical parameters of phobos. *Solar System Res., 48(4),* 269–278, DOI: 10.1134/S003809461404008X.

Nimmo F. (2004) Non-Newtonian topographic relaxation on Europa. *Icarus, 168(1),* 205–208, DOI: 10.1016/j.icarus.2003.11.022.

Nimmo F., Spencer J. R., Pappalardo R. T., and Mullen M. E. (2007) Shear heating as the origin of the plumes and heat flux on Enceladus. *Nature, 447(7142),* 289–291, DOI: 10.1038/nature05783.

Nimmo F., Bills B. G., and Thomas P. C. (2011) Geophysical implications of the long-wavelength topography of the Saturnian satellites. *J. Geophys. Res., 116,* E11001, DOI: 10.1029/2011JE003835.

Noyelles B., Karatekin O., and Rambaux N. (2011) The rotation of Mimas. *Astron. Astrophys., 536,* 1–13, DOI: 10.1051/0004-6361/201117558.

Ojakangas G. W. and Stevenson D. J. (1989) Thermal state of an ice shell on Europa. *Icarus, 81(2),* 220–241, DOI: 10.1016/0019-1035(89)90053-5.

Pang K. D., Voge C. C., Rhoads J. W., and Ajello J. M. (1984) The E ring of Saturn and satellite Enceladus. *J. Geophys. Res., 89(B11),* 9459, DOI: 10.1029/JB089iB11p09459.

Patthoff D. A. and Kattenhorn S. A. (2011) A fracture history on Enceladus provides evidence for a global ocean. *Geophys. Res. Lett., 38(18),* 1–6, DOI: 10.1029/2011GL048387.

Porco C. C. et al. (2006) Cassini observes the active south pole of Enceladus. *Science, 311(5766),* 1393–1401, DOI: 10.1126/science.1123013.

Postberg F., Kempf S., Schmidt J., Brilliantov N., Beinsen A., Abel B., Buck U., and Srama R. (2009) Sodium salts in E-ring ice grains

from an ocean below the surface of Enceladus. *Nature, 459,* 1098–1101, DOI: 10.1038/nature08046.

Postberg F., Schmidt J., Hillier J., Kempf S., and Srama R. (2011) A salt-water reservoir as the source of a compositionally stratified plume on Enceladus. *Nature, 474(7353),* 620–622, DOI: 10.1038/nature10175.

Rambaux N., Castillo-Rogez J. C., Williams J. G., and Karatekin Ö. (2010) Librational response of Enceladus. *Geophys. Res. Lett., 37(4),* 1–6, DOI: 10.1029/2009GL041465.

Rambaux N., Van Hoolst T., and Karatekin Ö. (2011) Librational response of Europa, Ganymede, and Callisto with an ocean for a non-Keplerian orbit. *Astron. Astrophys., 527,* A118, DOI: 10.1051/0004-6361/201015304.

Rappaport N. J., Iess L., Tortora P., Anabtawi A., Asmar S. W., Somenzi L., and Zingoni F. (2007) Mass and interior of Enceladus from Cassini data analysis. *Icarus, 190(1),* 175–178, DOI: 10.1016/j.icarus.2007.03.025.

Richard A., Rambaux N., and Charnay B. (2014) Librational response of a deformed 3-layer Titan perturbed by non-Keplerian orbit and atmospheric couplings. *Planet. Space Sci., 93–94,* 22–34, DOI: 10.1016/j.pss.2014.02.006.

Roberts J. H. (2015) The fluffy core of Enceladus. *Icarus, 258,* 54–66, DOI: 10.1016/j.icarus.2015.05.033.

Roberts J. H. and Nimmo F. (2008) Tidal heating and the long-term stability of a subsurface ocean on Enceladus. *Icarus, 194(2),* 675–689, DOI: 10.1016/j.icarus.2007.11.010.

Smith B. A. et al. (1982) A new look at the Saturn system:  The Voyager 2 images. *Science, 215(4532),* 504–537.

Soucek O., Hron J., Behounkova M., and Cadek O. (2016) Effect of the tiger stripes on the deformation of Saturn's moon Enceladus. *Geophys. Res. Lett., 43,* 7417–7423, DOI: 10.1002/2016GL069415.

Soucek O., Behounkova M., Cadek O., Tobie G., and Choblet G. (2017) Tidal deformation of Enceladus' ice shell with variable thickness and Maxwell rheology. In *19th EGU General Assembly,* EGU2017-16357.

Spahn F. et al. (2006) Cassini dust measurements at Enceladus and implications for the origin of the E ring. *Science, 311(5766),* 1416–1418, DOI: 10.1126/science.1121375.

Spencer J. R., Pearl J. C., Segura M., Flasar F. M., Mamoutkine A., Romani P., Buratti B. J., Hendrix A. R., Spilker L. J., and Lopes R. M. C. (2006) Cassini encounters Enceladus:  Background and the discovery of a south polar hot spot. *Science, 311(5766),* 1401–1405, DOI: 10.1126/science.1121661.

Spitale J. N. and Porco C. C. (2007) Association of the jets of Enceladus with the warmest regions on its south-polar fractures. *Nature, 449(7163),* 695–697, DOI: 10.1038/nature06217.

Squyres S. W., Reynolds R. T., Cassen P. M., and Peale S. J. (1983) The evolution of Enceladus. *Icarus, 53(2),* 319–331, DOI: 10.1016/0019-1035(83)90152-5.

Tajeddine R., Rambaux N., Lainey V., Charnoz S., Richard A., Rivoldini A., and Noyelles B. (2014) Constraints on Mimas' interior from Cassini ISS libration measurements. *Science, 346(6207),* 322–324.

Tajeddine R., Soderlund K. M., Thomas P. C., Helfenstein P., Hedman M. M., Burns J. A., and Schenk P. M. (2017) True polar wander of Enceladus from topographic data. *Icarus, 295,* 46–60, DOI: 10.1016/j.icarus.2017.04.019.

Thomas P. C. (2010) Sizes, shapes, and derived properties of the saturnian satellites after the Cassini nominal mission. *Icarus, 208(1),* 395–401, DOI: 10.1016/j.icarus.2010.01.025.

Thomas P., Burns J., Helfenstein P., Squyres S., Veverka J., Porco C., Turtle E., McEwen A., Denk T., and Giese B. (2007) Shapes of the saturnian icy satellites and their significance. *Icarus, 190(2),* 573–584, DOI: 10.1016/j.icarus.2007.03.012.

Thomas P. C., Tajeddine R., Tiscareno M. S., Burns J. A., Joseph J., Loredo T. J., Helfenstein P., and Porco C. (2016) Enceladus's measured physical libration requires a global subsurface ocean. *Icarus, 264,* 37–47, DOI: 10.1016/j.icarus.2015.08.037.

Tiscareno M. S., Thomas P. C., and Burns J. A. (2009) The rotation of Janus and Epimetheus. *Icarus, 204(1),* 254–261, DOI: 10.1016/j.icarus.2009.06.023.

Tobie G., Mocquet A., and Sotin C. (2005) Tidal dissipation within large icy satellites:  Applications to Europa and Titan. *Icarus, 177(2),* 534–549, DOI: 10.1016/j.icarus.2005.04.006.

Tortora P., Zannoni M., Hemingway D., Nimmo F., Jacobson R. A., Iess L., and Parisi M. (2016) Rhea gravity field and interior modeling from Cassini data analysis. *Icarus, 264,* 264–273, DOI: 10.1016/j.icarus.2015.09.022.

Travis B. J. and Schubert G. (2015) Keeping Enceladus warm. *Icarus, 250,* 32–42, DOI:10.1016/j.icarus.2014.11.017.

Tricarico P. (2014) Multi-layer hydrostatic equilibrium of planets and synchronous moons:  Theory and application to Ceres and to solar system moons. *Astrophys. J., 782(2),* 99, DOI: 10.1088/0004-637X/782/2/99.

Tyler R. (2011) Tidal dynamical considerations constrain the state of an ocean on Enceladus. *Icarus, 211,* 770–779, DOI: 10.1016/j.icarus.2010.10.007.

van Hoolst T. (2015) Rotation of the terrestrial planets. In *Treatise on Geophysics, 2nd edition, Vol. 10:  Physics of Terrestrial Planets and Moons* (G. Schubert, ed.), pp. 121–151. Elsevier, Amsterdam.

van Hoolst T., Rambaux N., Karatekin Ö., and Baland R. M. (2009) The effect of gravitational and pressure torques on Titan's length-of-day variations. *Icarus, 200(1),* 256–264, DOI: 10.1016/j.icarus.2008.11.009.

van Hoolst T., Baland R.-M., and Trinh A. (2016) The diurnal libration and interior structure of Enceladus. *Icarus, 277,* 311–318, DOI: 10.1016/j.icarus.2016.05.025.

Vienne A. and Duriez L. (1995) Ephemerides of the major saturnian satellites. *Astron. Astrophys., 297,* 588–605.

Waite J. H. et al. (2006) Cassini Ion and Neutral Mass Spectrometer:  Enceladus plume composition and structure. *Science, 311(5766),* 1419–1422, DOI: 10.1126/science.1121290.

Wieczorek M. A. (2015) Gravity and topography of the terrestrial planets. In *Treatise on Geophysics, 2nd edition, Vol. 10:  Physics of Terrestrial Planets and Moons* (G. Schubert, ed.), pp. 153–193. Elsevier, Amsterdam.

Wieczorek M. A. and Phillips R. J. (1998) Potential anomalies on a sphere:  Applications to the thickness of the lunar crust. *J. Geophys. Res., 103(E1),* 1715–1724.

Willner K., Oberst J., Hussmann H., Giese B., Hoffmann H., Matz K. D., Roatsch T., and Duxbury T. (2010) Phobos control point network, rotation, and shape. *Earth Planet. Sci. Lett., 294(3–4),* 541–546, DOI: 10.1016/j.epsl.2009.07.033.

Yin A., Zuza A. V., and Pappalardo R. T. (2016) Mechanics of evenly spaced strike-slip faults and its implications for the formation of tiger-stripe fractures on Saturn's moon Enceladus. *Icarus, 266,* 204–216, DOI: 10.1016/j.icarus.2015.10.027.

Zebker H. A., Iess L., Wall S. D., Lorenz R. D., Lunine J. I., and Stiles B. W. (2012) Titan's figure fatter, flatter than its gravity field. Abstract P23F-01 presented at 2012 Fall Meeting, AGU, San Francisco, California, 3–7 December.

Zharkov V. N. (2004) A theory of the equilibrium figure and gravitational field of the Galilean satellite Io:  The second approximation. *Astron. Lett., 30(7),* 496–507, DOI: 10.1134/1.1774402.

Zharkov V. N., Leontjev V. V., and Kozenko A. V. (1985) Models, figures, and gravitational moments of the Galilean satellites of Jupiter and icy satellites of Saturn. *Icarus, 61,* 92–100, DOI: 10.1016/0019-1035(85)90157-5.